Physica D 37 (1989) 359–383
North-Holland, Amsterdam

PATTERN SELECTION AND TRANSITION TO TURBULENCE IN PROPAGATING WAVES

Victor STEINBERG[a,b], Jay FINEBERG[a], Elisha MOSES[a] and Ingo REHBERG[a,*]
[a] *Department of Nuclear Physics, Weizmann Institute of Science, Rehovot 76100, Israel*
[b] *Center for Nonlinear Studies, Los Alamos National Laboratory, University of California, Los Alamos, NM 87545, USA*

We present a study of oscillatory convection in two experimental systems: ethanol–water mixtures in a rectangular container heated from below and a thin layer of nematic liquid crystals under low frequency ac voltage. In both systems the first bifurcation is the transition to traveling waves (TW) with finite wave vector and frequency. We report experimental observations of a sequence of spatial structures and dynamical behaviour of nonlinear TW in a regime of a weak nonlinearity. Most of the rich variety of spatial and dynamical behaviour which we observe in one-dimensional finite geometries has been reproduced by numerical simulations based on a simple model of coupled Ginzburg–Landau equations which considers only the combination of translation and finite geometry. More complicated spatio-temporal behaviour of TW in cells with two-dimensional geometry which initiated by defect nucleation is attributed to the mechanism of modulational instability of TW.

1. Introduction

In recent years it has become clear that despite the great success of dynamical system theory in quantitatively describing the temporal behavior of many nonequilibrium systems with suppressed spatial modes, systems with many spatial degrees of freedom, which are more common in the real world, cannot be characterized using these ideas. Early developments, as well as the following studies of large nonequilibrium systems, suggest that there are no universal routes to spatio-temporal chaotic behavior [1]. Several years ago a new approach to this problem was suggested, namely, to investigate a system which shows a transition to oscillatory instability as a first bifurcation [2]. Close to the onset the nonlinear behavior of such a system is described by a generalized Ginzburg–Landau equation with complex coefficients (GGL) which exhibits in some range of parameters a direct transition from a quiescent state to one of spatio-temporal turbulence [3],

$$\tau_0(\partial_t + s\partial_x)A = (1 + ic_0)\epsilon A + (1 + ic_1)\xi_0^2\partial_x^2 A - g(1 + ic_2)|A|^2 A. \quad (1)$$

Here ϵ is the system's control parameter (e.g. $\epsilon = R/R_c - 1$, where R is the Rayleigh number and R_c its threshold value), and τ_0, ξ_0 are the characteristic time and length respectively, s is the group velocity and g, c_0, c_1 and c_2 are real parameters. The complex amplitude, $A(x, t)$, describes the spatio-temporal modulation of the marginal waves. Since any system which shows oscillatory behavior falls in this class, and the corresponding instability mechanism is universal, we believe that universality in the transition to spatio-temporal chaos in this class of systems can be observed. This general idea has led to the recent renewal of interest in theory [4–13] and experiments [14–22] on Rayleigh–Bénard convection in a binary mixture since, as was shown theoretically and confirmed experimentally, this

*Permanent address: Physikalisches Institut, Universitat Bayreuth, D-8580 Bayreuth, Fed. Rep. Germany.

0167-2789/89/$03.50

system is a good candidate for the quantitative study of spatio-temporal complex behavior. Similar behavior has also been studied in Taylor–Couette flow [23], in oscillatory convection of a low-Prandtl number pure fluid [24] and in electroconvection of nematics [25].

There were several crucial experimental observations which attracted a great deal of attention among theorists and experimentalists. First, the observation of traveling waves (TW) in connecting binary mixtures in a finite geometry container [15, 16] made possible the study of properties that characterize a wide class of open flow systems, while using the well-controlled experiments achievable in closed systems. There are numerous examples of open flow systems which show the transition to spatially developing traveling waves, such as free shear flows (wakes, jets, mixing layers), plane Poiseuille and pipe flows, drift waves in plasma, etc. [26–32]. In most of these cases the GGL equation can be derived as a simple model to describe the nonlinear evolution of propagating patterns [3].

There are several specific features which characterize nonlinear behavior of propagating waves. The most distinct of them is the presence of two types of instability conditions: convective and absolute [33]. Unlike, e.g., stationary bifurcations where only an absolute instability exists, systems with broken O(2) symmetry can exhibit both convective and absolute instabilities. The difference between the two cases is a relative one in the sense that it depends on the choice of the reference frame in which the instability is considered. In the case of an absolute instability the perturbation grows in time at any fixed point in the system despite the fact that the wavepacket is advected downstream by the flow. In this case, any infinitesimal disturbance contaminates the entire flow, and temporal stability analysis describes how an initial spatial perturbation evolves in time. Then a solution of the corresponding dispersion relation with real wavenumber, k, and complex frequency, ω, is physically relevant. On the other hand, in convectively unstable systems, any initial perturbation is carried away by the flow such that at the initial site the medium is ultimately left undisturbed although the perturbation grows in a moving frame. In this case the spatial evolution of the perturbation with ω real and k complex, correctly describes the physical situation. Convective or absolute instability conditions depend on the relationship between the rate s/ξ_0 at which a perturbation is swept a distance ξ_0 downstream and a local growth rate τ_0^{-1}. The type of instability will, in turn, determine the pattern and temporal behavior selected by the system. In the framework of the GGL equation (1) it was shown [29] that the solution $A = 0$ becomes convectively unstable for $0 < \epsilon < \epsilon_t$, and absolutely unstable for $\epsilon > \epsilon_t = (s\tau_0/2\xi_0)^2(1 + c_1^2)^{-1}$. Thus a single nondimensional parameter $s^* = (s\tau_0/\xi_0)\epsilon^{-1/2}$ determines whether the system is convectively or absolutely unstable, and the transition from convectively to absolutely unstable conditions occurs [3] at $s_t^* = 2(1 + c_1^2)^{1/2}$. As a consequence of the convectively unstable condition the selected wavenumber, k^*, and frequency, ω^*, behind the front are [3]

$$k^* = \frac{\left(1 + c_1^2\right)^{1/2} \pm \left(1 + c_2^2\right)^{1/2}}{c_1 - c_2} \frac{\epsilon^{1/2}}{\xi_0} \tag{2}$$

and

$$\omega^* = \tau_0^{-1}(c_0 - c_1)\epsilon, \tag{3}$$

where k^* and ω^* are the deviations from the critical values k_c and ω_0 respectively. The selection mechanism behind the front is similar to one suggested for the vortex front propagation in, e.g., stationary Rayleigh–Bénard convection.

Cross [34, 35] used this idea of pattern translation to explain the variety of one-dimensional TW patterns observed in convecting binary mixtures in a finite container. Cross showed by numerical simulation of the coupled Ginzburg–Landau equations for left- and right-propagating waves with real coefficients that, similar to open flow systems, the patterns and dynamical behavior

which can be observed depend on the value of the non-dimensional group velocity s^*. It is astonishing that the rich variety of TW patterns predicted by the simulations have been independently observed experimentally in convecting binary mixtures: full-cell (saturated) nonlinear TW [15–17], spatially modulated TW (confined TW) [17, 36–39], spatially and temporally modulated TW (blinking TW) [40, 41] and nonlinear counter-propagating TW (CPW) [36, 37, 40]. Recently, this behavior has also been observed in different experimental systems [23, 24].

Another specific feature of the convectively unstable system is extreme sensitivity to external forcing. Moreover, the external noise modulation is selectively amplified by the system and spatially growing waves are generated at the frequency with maximum growth rate [42]. In relation to this feature noise-sustained structures and intermittency due to modulational instability of the nonlinear wavetrain downstream were observed in numerical simulations of the GGL equation at convectively unstable conditions [42, 43]. These specific features of spatio-temporal chaotic behavior distinguish the convectively unstable system from an absolutely unstable one.

Although we expected to find spatio-temporal chaotic behavior in one-dimensional systems as predicted for some range of parameters in numerical simulations of the GGL equation, we did not observe it. However, complex temporal behavior of wavenumber spectra and shock-like structures corresponding to rapid changes in wavenumber between two patterns with different k and ω were observed under convectively unstable conditions. This may point towards a modulational mechanism of secondary instability of TW which can lead to spatio-temporal chaos.

On the other hand, we discovered that slight variations in the cell width completely change the spatio-temporal behavior of TW; there is a direct transition to spatio-temporal chaotic behavior just near the convective onset in two-dimensional cells in a wide range of the control parameters [37]. These dynamics are elaborate, are characterized by the presence of different types of defects and cannot be described by low-dimensional attractors. A possible explanation of this behavior is related to modulational instability of TW; the dispersion of TW in the direction perpendicular to TW propagation dominates the pattern dynamics of TW and in a two-dimensional container spatially uniform envelopes are rarely stable [9, 10]. As mentioned in ref. [9] the cell does not have to be very wide in order to trigger the spatial instability along the TW crest. Thus modulational [44, 45], or Benjamin–Feir (BF) instability can produce the spatially and temporally incoherent flow observed experimentally, and the cell width is a crucial parameter which defines its onset. Recently similar spatio-temporal dynamics were obtained in numerical simulations based on the GGL equation [46] which suggest that the BF instability mechanism is very probable. One of the main issues is how to characterize two-dimensional spatio-temporal dynamics of TW and to compare them with numerical results.

The transition to spatio-temporal turbulence in convecting binary mixtures is complicated by a degeneracy of the wave vector in a horizontal plane. In electroconvection of nematic liquid crystals the wave vector direction is fixed due to the sample preparation procedure. Very large aspect ratios (up to a thousand wavelengths) can be reached in this system. This makes it very attractive for experimental studies of spatio-temporal pattern behavior. Moreover, we recently discovered that for some conditions the first bifurcation can be to ordered TW [47]. The great advantage of the TW state is that due to the raised degeneracy of the wave vector in a horizontal plane the transition from uniform TW to spatio-temporal turbulent state occurs through a simple scenario of defect nucleation [47]. Thus, this transition can be traced and studied quantitatively. Recent theoretical calculations and numerical simulations of the GGL equation which show surprising similarity to experimental observations of spatio-temporal pattern dynamics, suggest that this defect-initiated turbulent behavior (coined as topological turbu-

lence) is a direct manifestation of BF instability of TW in anisotropic systems [48–50]. It is the first step towards a universal route to spatio-temporal chaos.

In this paper we present recent experimental results on two systems: convection in binary mixtures and electroconvection in nematic liquid crystals (MBBA). Both systems show the first bifurcation from conductive state to a state with finite wave number and frequency. However, due to specific properties of these systems different manifestations of the TW states and their pattern dynamics were studied. The transition to the oscillatory instability in convecting binary mixtures has been studied in great detail by numerous theoretical groups during the last several years whereas there is no theoretical explanation for the transition to a TW state in nematics. The bifurcation in nematics is forward unlike the backward bifurcation in a convecting binary mixture. A simple estimate shows also that convectively unstable conditions for TW state in a nematics may be observed for $\epsilon \leq 0.001$, i.e. much closer to the convective onset than in binary mixtures and that we can reach at the moment in this system. Thus, pattern selection and spatio-temporal behavior under convectively unstable conditions in one-dimensional geometry cells were studied in binary mixtures while the universal transition to spatio-temporal disordered TW state was investigated in nematics.

2. Experimental systems

The apparatus used in the experiments on convection in binary mixtures was similar to that used in our previous work [36, 37, 51, 52]. The convective fluid layer is sandwiched between a water-cooled saphire window on the top and a hard nickel-plated copper mirror on the bottom. The lateral walls of the convection cell were constructed of various plastics chosen for their machinability as well as for their chemical resistance and thermal properties. Most of the cells we constructed from polypropelene which has low thermal conductivity [$\lambda = 1.2$ mW/(cm K)] and high density polyethylene with $\lambda = 5$ mW/(cm K). The cell frames were machined and polished to a uniformity in height of better than 5 μm. The top and bottom plates were checked interferometrically to ensure that they were parallel to within 1–2 μm on the cell's length. The heights of the cells were $d = 0.300$ cm and 0.305 cm and the lateral dimensions in units of d are $4 \times \Gamma$, where the aspect ratio Γ ranges from 12 to 12.7, as well as 20 and 27. Long term temperature stability of the bottom plate was about 0.03 mK RMS so that we were able to get relative stability in the Rayleigh numbers on the order of 10^{-5} RMS.

The experiments were done on ethanol–water mixtures with weight concentrations of ethanol in the range between 25.5% and 28.5% at 31°C mean temperature. For this range of ethanol concentration the separation ratio ψ varied from -0.078 to -0.005, the Prandtl number was a constant, $P = 18$, and the Lewis number was $L = 0.012$ [53]. We also used a benzene–methanol solution of 95% by weight concentration of benzene at 30.2°C ($\psi = -0.045$, $P = 7.5$, and $L = 0.025$). The apparatus described above enabled us to make simultaneously high resolution heat transport measurements (Nusselt number, N, measurements) with resolution on the order of 0.01% and precision shadowgraph measurements. We use conventional shadowgraph flow visualization with the image obtained directly by a video camera. Since we worked in the linear region of the shadowgraph close to the convective onset the optical signal obtained at a given point was linearly proportional to the amplitude of the velocity field (or related to it the temperature and concentration fields). A computer-based image-processing system provided a standard image enhancement, noise filtering and reduction techniques for the study of the evolution of spatio-temporal flow patterns.

The experimental setup for electroconvection in nematics is the standard one [54, 56]: the nematic MBBA is sandwiched between two transparent glass electrodes a distance of 15 μm apart and

lateral dimensions of the cell $L_x = 2$ cm (perpendicular to the rolls) and $L_y = 0.5$ mm (aspect ratio 1 : 33 : 1300). The cell is regulated at 25°C with a stability of ± 0.005 K by circulating water flow. With proper sample handling and preparation this temperature regulation turns out to be the crucial factor in reaching reasonable short-term stability and reproducibility within several hours [47]. However, sample aging during several weeks was still observed. The image of the patterns is observed with a video camera mounted on a polarizing microscope digitized with a resolution of 512×512 pixels of 256 grey scales and fed to a computer.

3. Results

3.1. *Oscillatory convection and TW in binary mixtures*

In a binary fluid the control parameters which determine the convective flow are the Rayleigh number, R, which is proportional to the temperature difference across the fluid layer, ΔT, and the separation ratio, ψ, which is a measure of the coupling between the temperature and concentration gradient, induced by the Soret effect. Other relevant parameters are the Prandtl number, $P = \nu/\kappa$, and the Lewis number, $L = D/\kappa$, where ν is the kinematic viscosity, and D and κ are the mass and thermal diffusivities, respectively [56, 57]. For $\psi \leq -L^2$ the concentration gradient stabilizes the quiescent state and leads to an oscillatory instability. The critical Rayleigh number for the onset of the oscillatory instability R_{co} is defined approximately as [56, 57]

$$\frac{R_{co}}{R_c} = 1 - b\psi/(1 + \psi + P^{-1}) \qquad (2)$$

and the neutral frequency of marginal waves is given approximately by [56, 57]

$$\omega_0 = (3a\pi^2/2)\left[-\psi/(1 + \psi + P^{-1})\right]^{1/2}. \qquad (3)$$

Here R_c is the eigenvalue of the linear stability problem for stationary convection, ω_0 is considered in units of the vertical thermal diffusion time, $t_v = d^2/\kappa$, where d is the cell height. For free, permeable boundary conditions the formulas (2) and (3) are exact with $a = b = 1$. For rigid, impermeable boundaries, eqs. (2) and (3) are a good approximation with $a = 1.43$ and $b \simeq 1.05$ (ref. [56]). Exact numerical calculations for realistic boundary conditions have been performed recently by several groups and are in excellent agreement with experiments [58–60]. Recent visualization experiments revealed that linear oscillatory convection predicted by linear stability analysis can be observed in a transient regime and, in fact, is only neutrally stable [61, 62]. This state is observed experimentally in the form of two counter-propagating waves (CPW) whose amplitudes grow exponentially along their propagation direction [61]. Combined effects of propagation, refection and growth cause the onset shift which depends on boundary conditions at lateral walls and the cell length [34]. All these properties of linear CPW were verified experimentally [61, 62]. The temporal behavior of the linear transient state was first studied long ago and the results were also found to be in reasonable agreement with the theory [63]. The unresolved problem of an almost negligible change in the effective heat transport in the linear growth-rate regime of CPW, first mentioned in ref. [63] and confirmed by us, was also resolved recently [64]. The solution is the greater resolution of local optical as compared with global heat transfer measurements; careful data analysis show similar linear growth-rate behavior in both measurements in the transient regime. Thus, the linear oscillatory state is now well understood quantitatively. As mentioned above the linear CPW are unstable; their amplitudes grow exponentially until limited by nonlinear saturation. The amplitude profiles flatten out and become more like two distinct CPW emanating from the source [36]. This meeting point of CPW is a topological defect which is one of two possible singular solutions of GGL equations. This

state with the source defect is unstable to small perturbations (slight asymmetry of the cell imperfections, etc.), and the defect moves toward one of the end walls. The migration of the topological defect along the cell is not smooth and regular but occurs by jumps of the order of half a wavelength. The existence and stability of the source and sink topological defects as singular solutions of the GGL equation were considered theoretically [65, 66], and their stability and dynamics are similar to experimental observations [36, 37]. Moreover, the defect migration by jumps can be explained by nonadiabatic effects of the sub-critical oscillatory bifurcation which can result in the pinning of TW [67].

Our experiments show that a large step in the Rayleigh number above the onset leads via a subcritical bifurcation to nonlinear TW filling the cell while smaller steps lead to weakly nonlinear states which exhibit a large variety of flow patterns [36]. The appropriate question is how to characterize these two different regimes particularly in the simplest case of a one-dimensional geometry where three-dimensional effects can be neglected. Since we deal with a subcritical bifurcation it is difficult to define a region of applicability of one mode approximation based on the value of the order parameter (or amplitude) or the control parameter ϵ. It is reasonable to assume however that the frequency of the oscillation, which in the linear state is directly related to the vertical linear concentration profile, can play the role of the parameter which characterizes the degree of deviation from linear behavior. Thus, weakly nonlinear states have oscillation frequencies that are only slightly different from the neutral frequency while for the nonlinear TW this difference can be an order of magnitude in the range of ψ in which we worked [16, 17, 36, 37]. This means that convective flow perturbations of the linear vertical concentration profile of the conduction state are small in a weakly nonlinear regime. It was suggested in ref. [41] that the small distortion of the concentration profile is due to the fact that in the region where $\epsilon \leq L^2$ the characteristic boundary layer is comparable to the cell height. First, our measurements show a reduction of 10 to 15% in the frequency for ϵ values up to $\epsilon = 5 \times 10^{-3}$, much higher than the value of L^2 ($\simeq 10^{-4}$). Secondly, as we discovered, mass transport onset coincides with the onset of the weakly nonlinear state, i.e. mass transport due to nonlinear TW leads to the breaking of the linear concentration profile [68–70]. Such an effect will dominate over any boundary layer process since the latter depends on changes in the velocity amplitude of the roll which are small along a weakly nonlinear branch [16, 17].

Thus, the weakly nonlinear states are close to the linear ones due to relatively small amplitudes and the small deviation of frequencies from the neutral frequency, ω_0 [40, 41]. This means that standard perturbation analysis can be applied to describe these states. Cross used this approach taking into account only the effects of pattern propagation [34, 35]. Using coupled GL equations with real coefficients for left- and right-propagating waves he performed numerical calculations in a finite geometry cell with realistic boundary conditions on the lateral walls. The linear part of the equations gives a complete quantitative description of the dynamical and spatial structure of the linear oscillatory state in a finite geometry cell. As a result of energy losses due to reflections the theory predicts a shift in the convective onset ϵ_s which is inversely proportional to the cell length and depends on the reflection coefficient [34]. Depending on the value of the nondimensional group velocity s^* Cross obtained a variety of static and dynamic states which he classified [35]. The maximum value of the group velocity s^* is obtained at onset and depends on the lateral boundaries and the length [35]:

$$s_s^* = \frac{s\tau_0}{\xi_0 \epsilon_s}, \tag{4}$$

where $\epsilon_s = -(s\tau_0/l)\ln|r|$ is the shift, l is the cell length and r is the reflection coefficient. The highest value of s_s^* observed in our experiments is 2.6

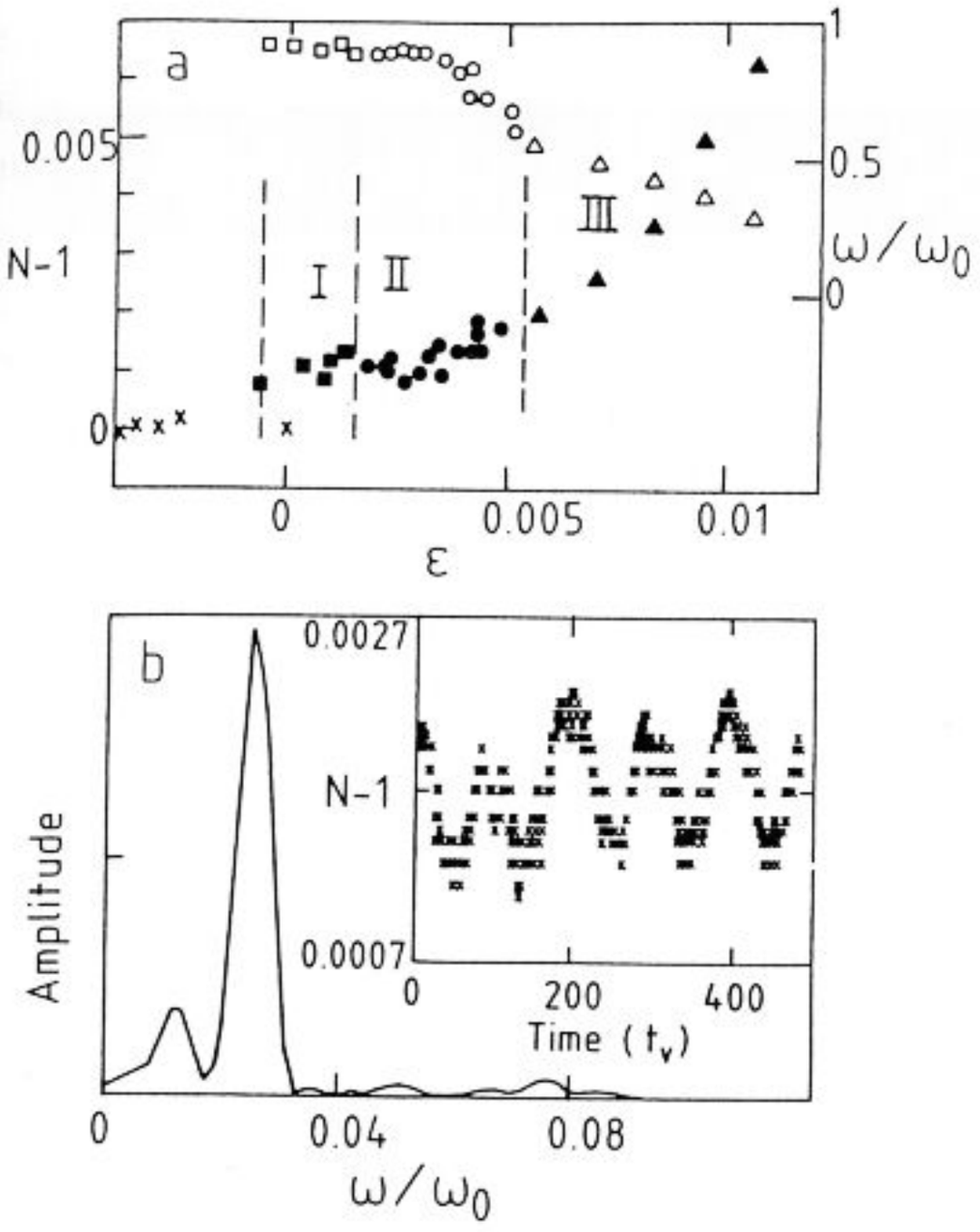

Fig. 1. (a) Steady state Nusselt number, N, and scaled TW frequency, ω_1/ω_0 as a function of ϵ. Vertical lines define regions of different nonlinear TW patterns: I: stable nonlinear CPW (squares); II: blinking states (circles); III: confined TW (triangles). Crosses show the conduction state. N and ω_1/ω_0 are shown by full and empty symbols respectively. (b) N for the blinking states (region I) as a function of time and its power spectrum at $\epsilon = 0.0034$ with $\psi = -0.014$ in an ethanol–water mixture.

at $\psi = -0.058$ and $\Gamma = 20$. The sequence of patterns observed as a function of decreasing values of s^* is as follows:

1) For the highest values of s^* a symmetric state of right and left TW was observed which resembles the linear transient CPW but is actually a stable nonlinear state of the system (fig. 1(a) of ref. [71])

2) As s^* decreases, the patterns consists of left and right TW with amplitudes different from each other. The symmetry is broken and one of the waves dominates (fig. 1(b) of ref. [71]).

3) At smaller s^* a transition to symmetric oscillations of the two envelopes is observed with a modulation period much longer than the internal TW period ("blinking" state) (fig. 1(c, d) of ref. [71]).

4) A further decrease in s^* causes the state to once again become asymmetric. The modulation period decreases further with decreasing s^* and is incommensurate with the internal TW frequency so that the overall state is quasiperiodic as in the previous state. For smaller values of s^* (higher values of ϵ) aperiodic (chaotic) states are also observed (fig. 1(e, f) of ref. [71]).

5) Finally, in the region of $s^* \geq 2$ the modulation ceases, and either a left or right propagating TW state remains. The envelope of the state is spatially modulated so that this state resembles a kink-like pattern ("confined" state) (fig. 1(g) of ref. [71]). On the branch at $s^* < 2$ there is a transition to a spatially homogeneous TW which completely fills the cell (fig. 1(h) of ref. [71]) (filling, or saturated TW).

As mentioned in the introduction, the sequence of TW states listed above corresponds to experimentally observed states in the close vicinity of the convective threshold. We will present next experimental observations of the weakly-nonlinear states in the same order of decreasing values s^* (or increasing values of ϵ).

The regions of existence of the various nonlinear states for the ethanol–water mixture at $\psi = -0.014$ is presented in the plot of the Nusselt number (N) versus ϵ for measurements in the close vicinity of the convective threshold (fig. 1(a)). In the same figure characteristic internal frequencies ω of the various TW states, normalized by the neutral frequency ω_0 are also presented (fig. 1(a)). The data were taken for a polypropelene-walled cell with aspect ratio 12. A small step from the conduction state ($\epsilon \leq 2 \times 10^{-4}$), a transition to the nonlinear states occurs with a discontinuous change in N on the order of 0.1%. The transition appears by way of the transient linear CPW with the observed frequency $\omega_0 = 2\pi f_0 t_v = 2.505$ which is close to the calculated value of $\omega_0 = 2.5$ ($t_v = 90.6$ s).

Fig. 2 shows the maximum amplitude of the shadowgraph signal for all three weakly nonlinear TW states as a function of ϵ for the same set of data as in fig. 1 ($\psi = -0.014$ and $\Gamma = 12$). There is

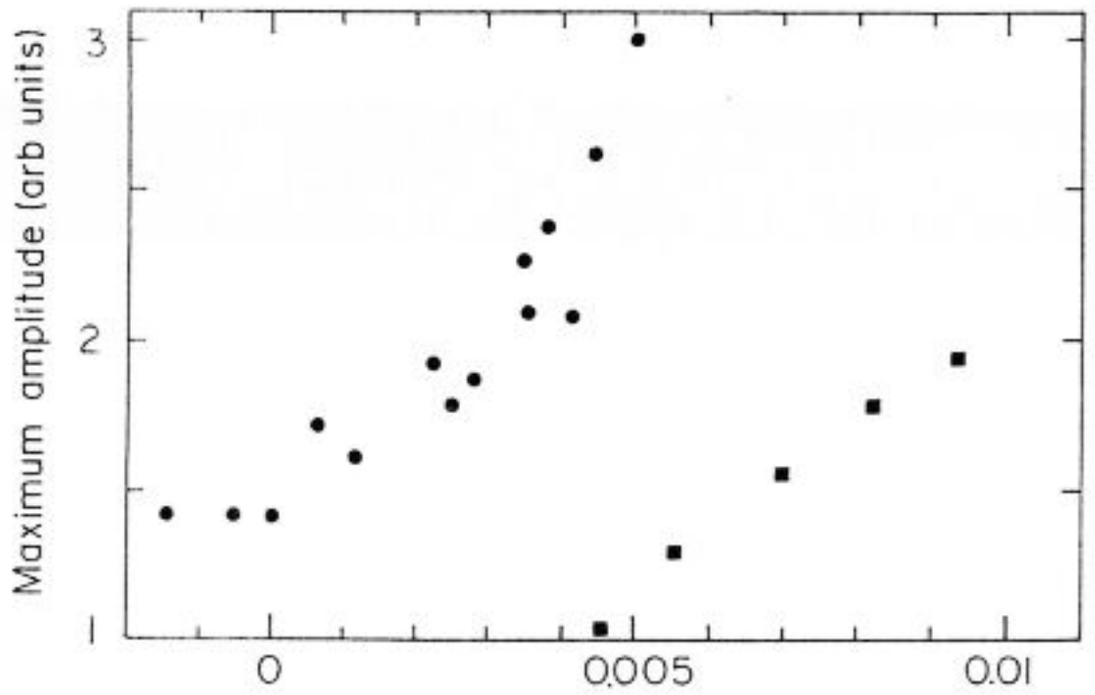

Fig. 2. The maximum amplitude of each state as a function of ϵ for $\psi = -0.014$ (circles), blinking and CPW states (squares) confined states -0.014.

a noticeable jump in the maximum amplitude at the transition between the blinking and confined TW states although no such jump is observed for the transition between the nonlinear CPW and the blinking state. The sharp rise in the maximum amplitude of the blinking state and the jump at the transition to the confined state were also observed for $\psi = -0.058$ although the size of the jump was smaller. In the region marked I in fig. 1(a) the nonlinear CPW appears first, then the blinking TW state occurs in region II, and the confined TW is in region III. In terms of s^* we find that for the data in fig. 1(a), the nonlinear CPW exist for $2.12 > s^* > 1.94$, the blinking states for $1.94 > s^* > 1.69$, and the confined states for $1.69 > s^* > 1.5$. Thus, we observed nonlinear TW states which strongly resemble those which have been observed in numerical calculations but at considerably higher values of s^*.

Since the transition to nonlinear finite amplitude TW states is of a subcritical nature one would expect hysteretic behavior. Unfortunately, the problem of hysteresis is a tricky one, and in the case of the confined TW, was discussed by us elsewhere [72] (see next sections also). The existence of the nonlinear CPW and blinking states depend heavily on reflection effects at the lateral boundaries of the cell [72]. The convective onset $\Delta T_c(\text{exp})$ have been found to be in good agreement with the calculated threshold in the finite geometry container and depends on ψ, the cell length and lateral boundary conditions. The confined TW branch is unaffected by the location of $\Delta T_c(\text{exp})$ and appears to be more hysteretic relative to $\Delta T_c(\text{exp})$ if the critical threshold is shifted toward higher temperature differences [72] due to the boundary conditions or to the cell length. If $\Delta T_c(\text{exp})$ is shifted to values lower than a saddle node of the confined TW branch the lower lying blinking TW and nonlinear CPW states will be observed. Thus, these states, observed at higher values of s^*, are highly dependent on the location of $\Delta T_c(\text{exp})$. We checked this statement experimentally by varying the cell length and lateral boundaries and were able to observe the lower lying TW states at $\psi = -0.058$ in a long cell ($\Gamma = 20$) with walls of poor thermal conductivity. This explains why weakly nonlinear states have not been seen until recently [40, 41]. Concerning the hysteretic behavior of the lower lying TW states, we recently found that the most hysteretic states for the nonlinear CPW and blinking TW are observed at $\epsilon = -5 \times 10^4$, -8×10^{-4}, -1.3×10^{-3}, and -2×10^{-4} for values of $\psi = -0.014$, -0.015, -0.020 and -0.058, respectively. A considerably larger hysteretic region, shown in fig. 3(a) of ref. [40] was incorrect: part of the hysteretic states on subsequent evaluation were found to be unstable transients with long relaxation times [73]. This lack of hysteresis, also observed in ref. [41], definitely requires a theoretical explanation.

In the following sections we present a detailed description of each of these three weakly nonlinear branches.

3.1.1. *Nonlinear CPW (symmetric nonlinear TW)*

This lowest nonlinear TW state observed in region I of fig. 1(a) consists of two symmetric left and right TW whose envelopes are time independent. The intensity of the shadowgraph signal taken as a function of position along the convection cell at a sequence of time interval of $0.66t_v$ is shown in fig. 3. The oscillation period of the nonlinear CPW is $2.196t_v$ at $\epsilon = 0.001$. This plot is very similar to one corresponding to the transient

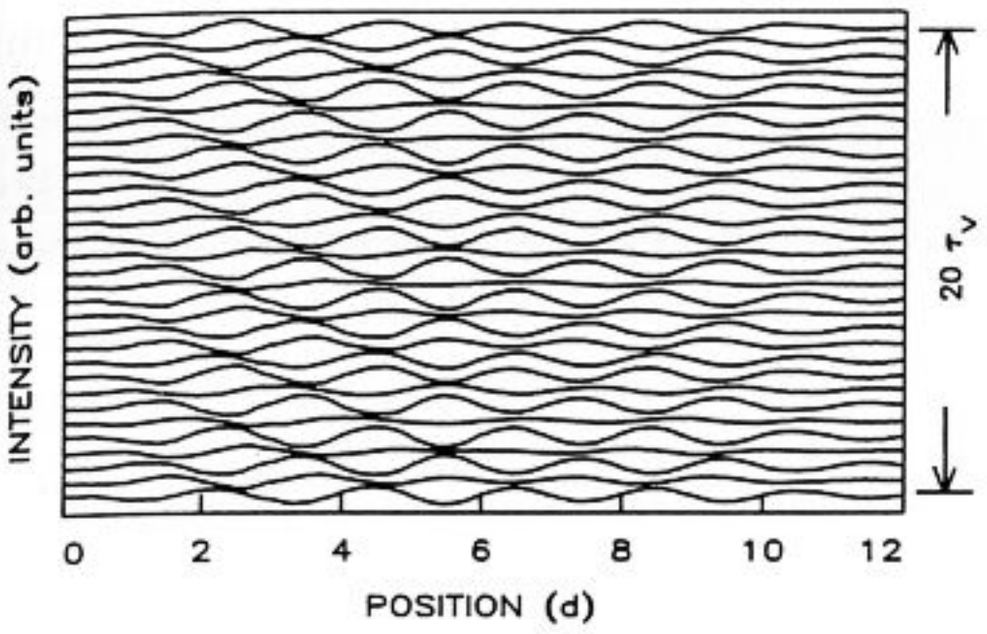

Fig. 3. The contour plot of a stable nonlinear CPW state. This state was observed at $\psi = -0.014$ for a PP cell with aspect ration, $\Gamma = 12$, at $\epsilon = 0.001$.

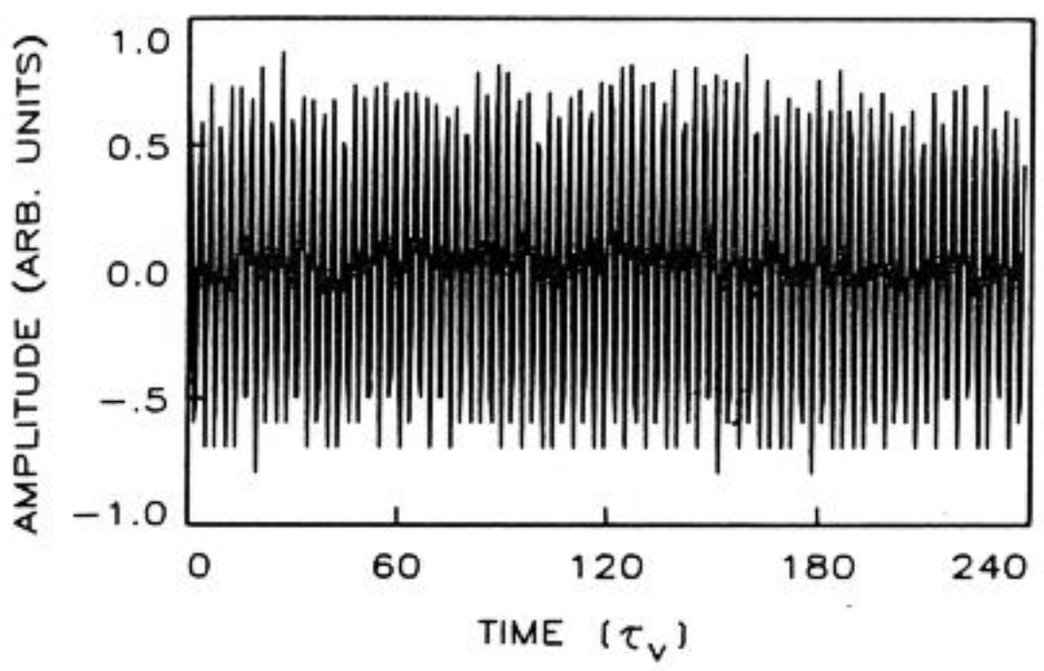

Fig. 4. The amplitude at one spatial point as a function of time for the state shown in fig. 3.

linear TW. The intensity of the shadow-graph signal taken at one point in the cell as a function of time is shown in fig. 4 and demonstrates the time independence of the nonlinear CPW envelope function. Finally, in fig. 5 the power spectrum of the data in fig. 4 shows a single peak with a frequency of $0.897\omega_0$.

We would like to mention here that in spite of the fact that no other peaks or harmonics are evident in the CPW frequency spectrum, a time-dependent wavenumber spectrum of this state at an average wavenumber $\bar{k} = k_c$ (k_c is the critical wavenumber for linear TW) was observed. Both the temporally modulated wavenumber spectrum and a range of variation of k can be described well by a simple linear superposition model suggested by Kolodner [74]. The physics of the time dependence on the fast time scale on the order of a half cycle of the oscillations is probably

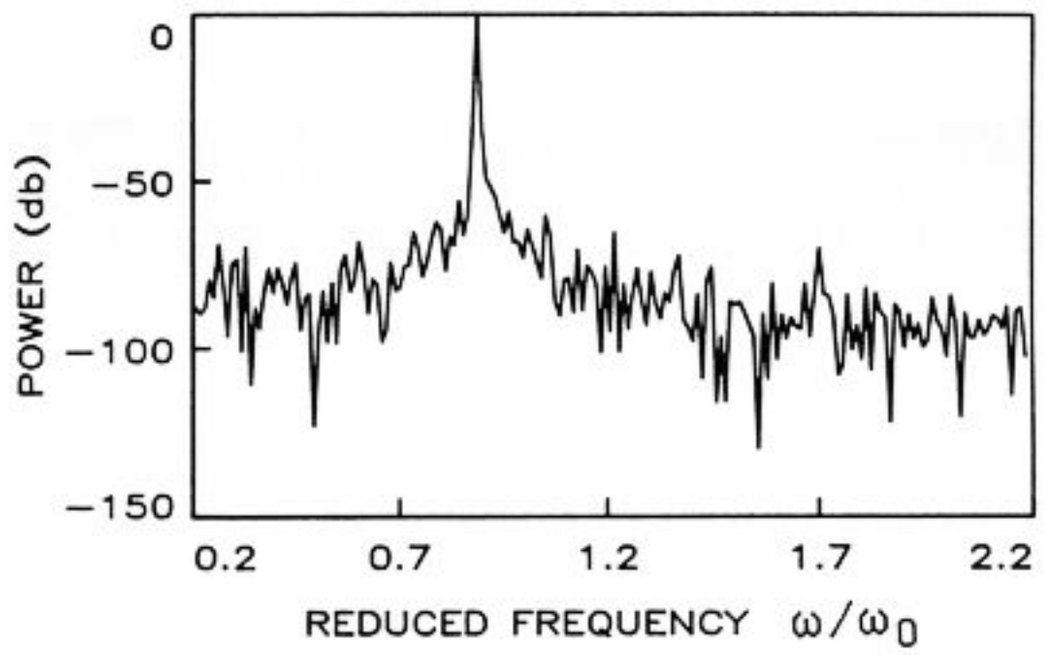

Fig. 5. The power spectrum of the data presented in fig. 4, only one peak is observed.

related to pinning of the spatial phase of the wave in the cell center and to periodically stretching it toward the ends of each half cycle. It is not clear, however, why this temporal modulation was not observed in the transient linear CPW in the same experiment.

3.1.2. *Spatially and temporally modulated TW (blinking state)*

The next lower lying weakly nonlinear TW state is a spatially and temporally modulated TW state which persists along the nonlinear branch for a range of about $\Delta\epsilon \simeq 0.006$ (region II) until a continuous, non-hysteretic transition to the confined TW state occurs (region III) (fig. 1(a)) as measured in both heat transport and oscillation frequency. Time dependence in heat transport due to the amplitude modulation in region II of fig. 1(a) was reduced by averaging for several hours; nevertheless the scatter remains relatively large. The time dependence of the Nusselt number for $\epsilon = 0.0054$ is illustrated in fig. 1(b) where $N - 1$ as a function of time (inset) and its power spectrum are shown. The slow time scale characterizing the "blinking" period of the state's envelope is seen by the location of the peak at $\omega_2 = 0.02\omega_0$. As shown by the data at the top of fig. 1(a), the basic TW frequency ω_1, of the blinking state is within 10–15% of the neutral frequency, ω_0. In addition ω_1 closely follows the changes in N over the entire branch.

In fig. 6, shadowgraph pictures of the blinking state at a constant value of $\epsilon = 5.6 \times 10^{-4}$ for $\psi = -0.020$, are shown at intervals of $\Delta t = 6.6 t_v$; approximately half of a blinking cycle is shown. The patterns are seen in the figure to be truly one dimensional. Details of the dynamics of the state are presented, for $\psi = -0.014$ and $\epsilon = 0.0048$, by light intensities measured along the cell length and plotted on top of each other with time intervals of $0.66 t_v$ (fig. 7). At the beginning of the modulation period this TW state is confined to one side of the cell, propagating in the direction of a lateral wall (fig. 7(a)). It then starts to fade as another TW propagating in the opposite direction appears (fig. 7(b)), and finally the amplitude of the TW propagating in the other direction grows while the TW amplitude on the other side decays completely (fig. 7(c)). This cycle then repeats itself. This behavior corresponds exactly to Cross's observations based on his numerical simulations [35].

The time-dependent behavior of the blinking state is illustrated in fig. 8 by plotting the measured shadowgraph intensity at one point as a function of time. As ϵ increases above the convective threshold, the oscillation amplitude grows exponentially. This transient CPW state reaches saturation as the state's amplitude becomes temporally modulated (fig. 8(a)). Fig. 8(b, c) shows several modulation cycles of the blinking state for low values of ϵ in a steady state region (after the transient decays) for the ethanol–water mixture. The frequency of the slow modulation is nearly constant and much slower than the internal TW frequency. Shown are data taken at both the left and right ends of the cell, and, as can be seen from the figures, the modulations at each end of the cell are clearly not in phase, although they reach the same value of the peak amplitude, i.e. both waves are modulated symmetrically, but at large ϵ asymmetric modulations are also observed.

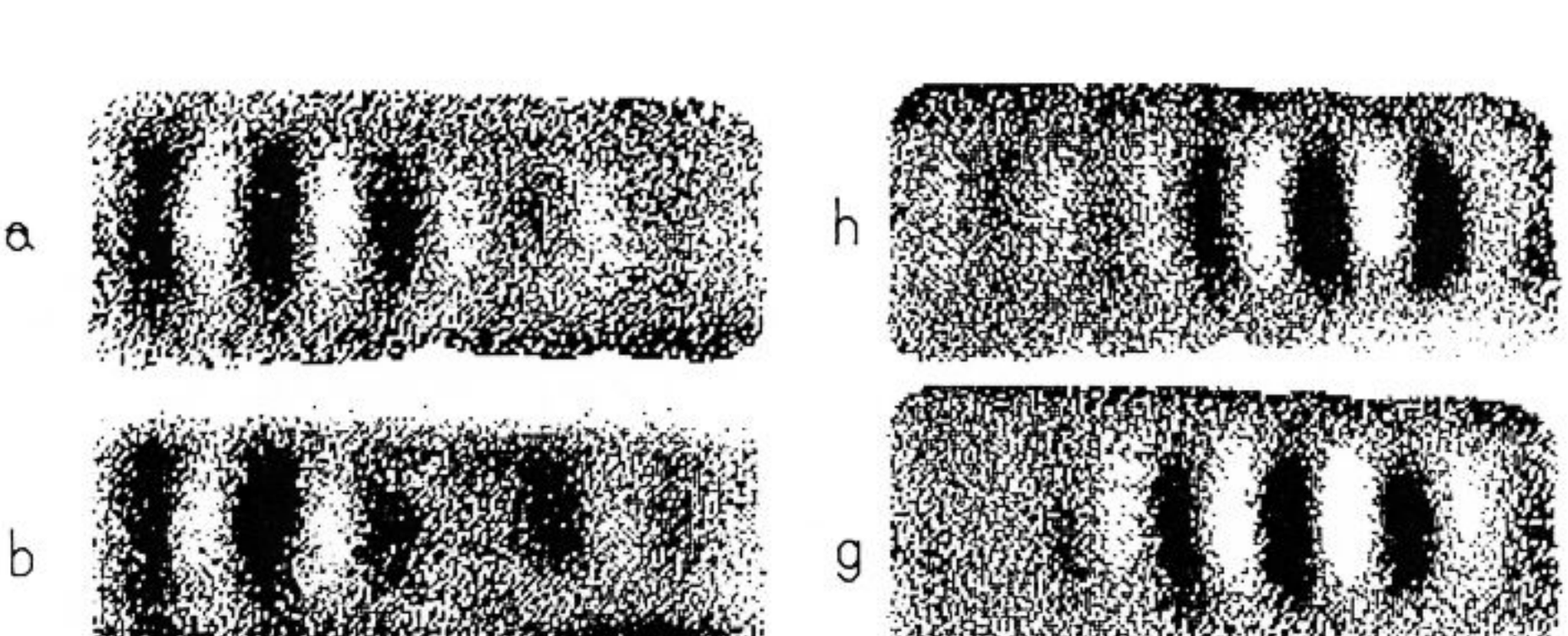

Fig. 6. A series of shadowgraph pictures showing a blinking state at $\psi = -0.020$, a constant $\epsilon = 5.6 \times 10^{-4}$. The pictures starting from (a) are taken consecutively with a time interval between pictures of $6.6 t_v$. Approximately half a cycle is shown.

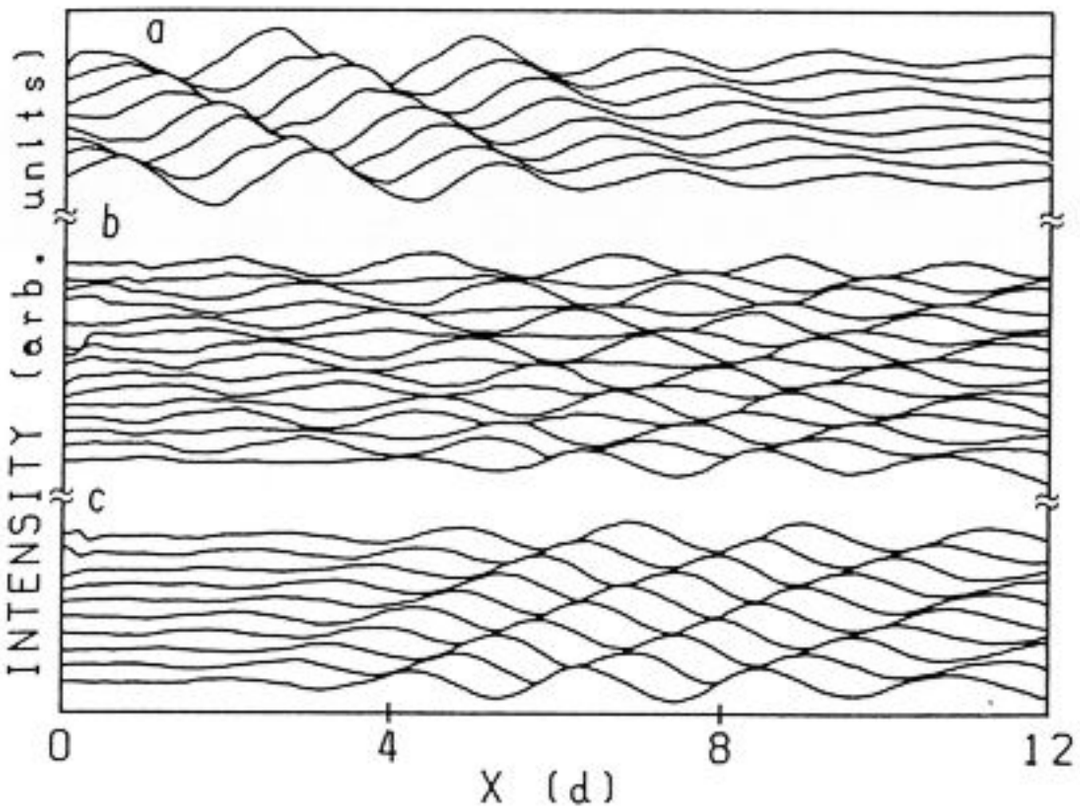

Fig. 7. A contour plot of shadowgraph signals for the blinking state taken at $\psi = -0.014$ in an ethanol–water mixture as a function of position along the cell. Each line is a profile of the state, taken along a line extending the length of the cell at sequential time intervals of $0.66t_v$. Time increases upwards. The plots are taken at times: bottom $0t_v$, center $66t_v$ and top $106t_v$.

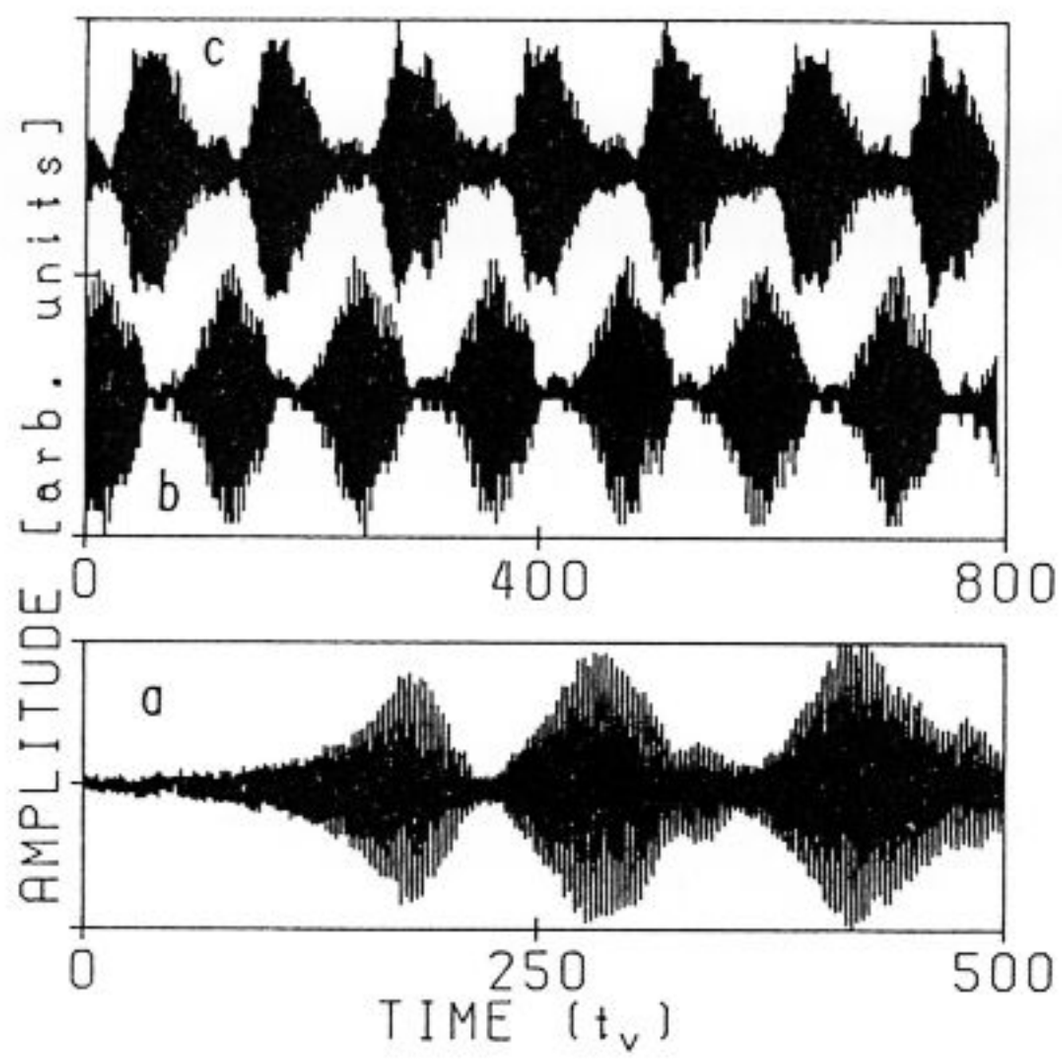

Fig. 8. Bottom: the intensity of the shadowgraph signal at one point as a function of time as ϵ increases from conduction to a value of 0.0009 at $\psi = -0.014$. Top: several cycles of the blinking state for $\psi = -0.020$ and $\epsilon = 2 \times 10^{-4}$ for points taken concurrently at the left (lower) and right (upper) sides of the cell.

This steady state scenario is typically reached after relaxation times on the order of several horizontal diffusion times which, for the longer $\Gamma = 20$ cell, can reach 30–40 hours. This regular modulation cycle for the small ϵ state is not the case for higher values of ϵ. In fig. 9 we present the time dependence of the shadowgraph intensity taken at one point for these more complicated states. The behavior of these states is seen to be very irregular in contrast to the clocklike behavior shown in fig. 8(b, c).

In fig. 10 we present power spectra of the shadowgraph signal intensity taken at points situated at opposite sides of the cell during the blinking cycle as a function of ϵ for $\psi = -0.020$. The spectra low on the branch are quasiperiodic indicating a two-frequency state. (This should be compared to the spectrum shown in fig. 5 for the CPW state which consists of only one peak). The peak separation is discrete and corresponds to the blinking frequency, ω_2, of the state. In general, as ϵ increases we find that the blinking frequency, ω_2, decreases. All peaks in the spectrum can be given as an integer combination of two neighboring peaks. Very low on the branch (fig. 10(a, b)), the main peak at ω_1 is identical on both sides of the

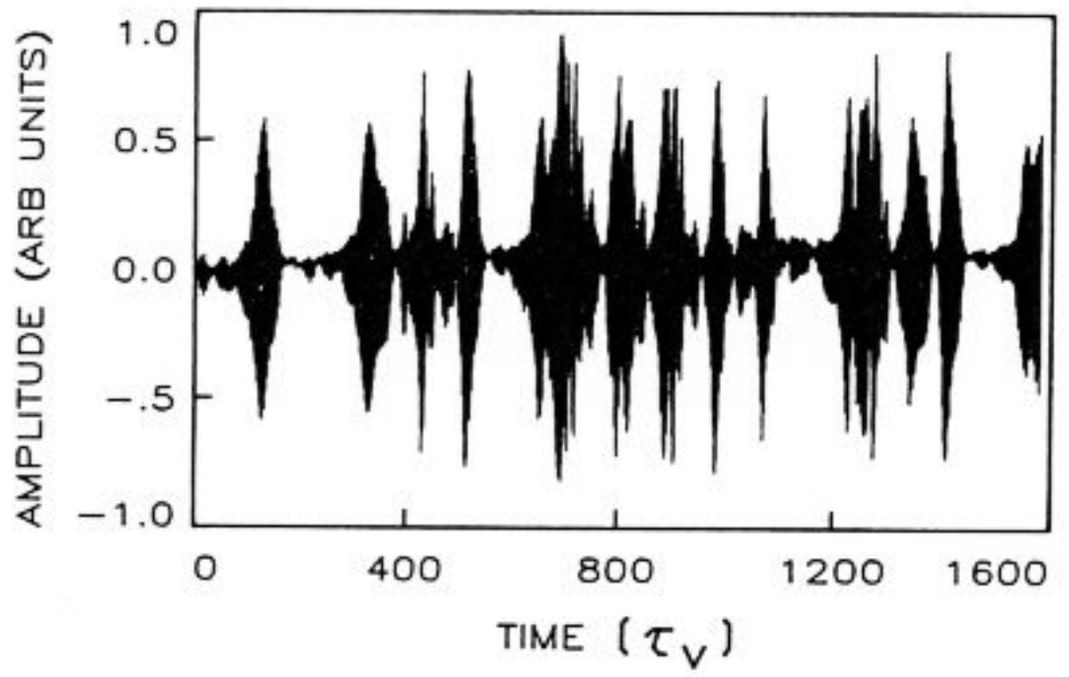

Fig. 9. The shadowgraph amplitude at one point for an aperiodic blinking state. The state shown was observed for $\psi = -0.058$ at $\epsilon = 0.0031$.

cell. Higher up on the branch (fig. 10(c)) the main peaks at the cell's end separate. Each spectrum is in turn quasiperiodic. This separation of the spectra at the two ends of the cell is the first indication of the breaking of the left–right symmetry of the system observed in numerical simulations [71]. This is the beginning of the dominance of one direction over the other and is in competition with the role of reflection at the

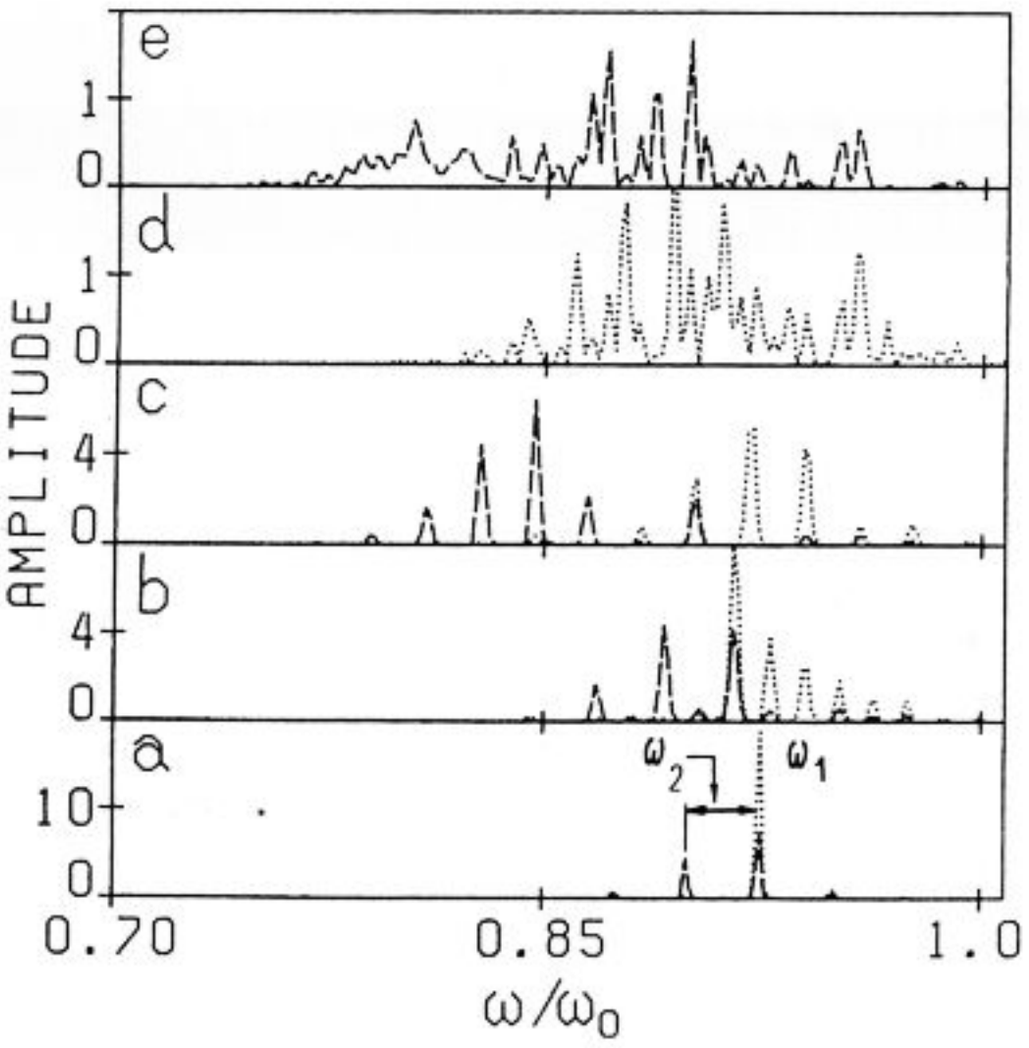

Fig. 10. Power spectra of the shadowgraph signal for the blinking TW state taken at points situated at each end of the cell. Dotted line: spectra taken at a point on the right of the cell. Dashed line: spectra taken at a point on the left of the cell. All spectra shown were taken for $\psi = -0.020$. (a) $\epsilon = -0.0013$; (b) $\epsilon = -5.0 \times 10^{-4}$; (c) 2.6×10^{-4}; (d) 7.8×10^{-4}.

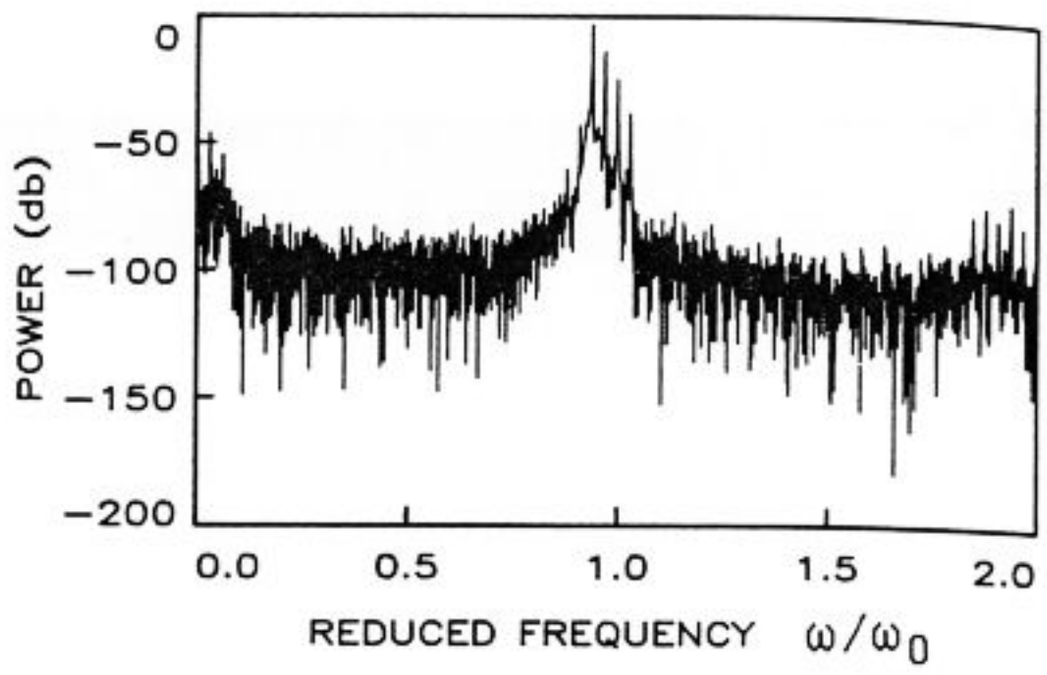

Fig. 11. The power spectrum of the time dependence of one spatial point for a blinking state observed for $\psi = -0.058$ at $\epsilon = 0.002$.

boundaries which in effect tries to restore this symmetry. This domination eventually culminates in the strongly nonlinear states where one direction completely dominates the dynamics. Still higher on the branch (fig. 10(d, e)) the spectra become more complicated but are still discrete as the simple two-frequency quasiperiodic state evolves into a more complex one.

The blinking state branch ends at a continuous transition to the confined state branch. At this point the power spectrum narrows to a single sharp peak. The lower and higher parts of the spectra in fig. 10 are not shown since their amplitudes are several orders of magnitude smaller than the spectra in the figure. For completeness, we present in fig. 11 the entire spectrum corresponding to a simple, 2-frequency blinking state. As can be seen from the figure, the entire spectrum consists of a small number of discrete peaks whose frequencies are very close. Peaks of much lower amplitude corresponding either to harmonics of the main peaks or to their sums and differences in frequency.

Higher on the branch the complicated modulated TW states may correspond to either the three-period quasiperiodic states or the chaotic states observed numerically by Bestehorn et al. [46]. We performed dimensional analysis on the data whose spectra are presented in fig. 10, using the Grassberger–Procaccia algorithm [75] to determine the correlation dimension, D, of their associated attractor. We do not expect that the results of this analysis are in any way rigorous due to the relatively small (typically 2000–4500 points) size of the data sets, but we are able to gain some qualitative intuition about the underlying behavior of the attractors. We found that D jumps from a dimension of $D \approx 2$ which we would expect for a simple, two-frequency, quasiperiodic attractor, to $D \lesssim 3$ for the more complicated behavior exhibited at higher values of ϵ. This suggests that these states, although aperiodic, with complex, but still discrete spectra indeed correspond to a low-dimensional attractor. Results of this analysis are presented in fig. 12 for the data set presented in fig. 9 for various imbedding dimensions. The solid line in the figure is a line of slope 3 and is shown for comparison with the data. The scaling region of the plot is consistent with an attractor of this dimension.

Two other striking features of the blinking state are a jump in the average wavenumber about $0.07k_c$ at the transition from the nonlinear CPW and the variation of the wavenumber as a function

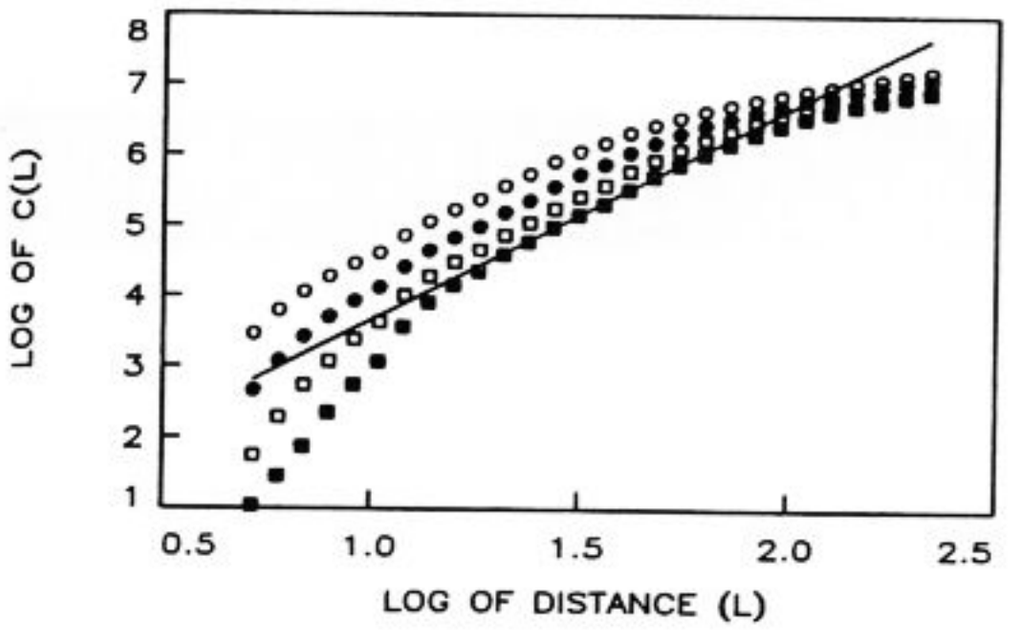

Fig. 12. Dimensional analysis of the aperiodic blinking state shown in fig. 9. Shown are the results for imbedding dimensions 7 (empty circles), 9 (full circles), 11 (empty squares) and 13 (full squares). The slope of the lines shown gives the correlation dimension of the attractor. The solid line for reference has a slope of 3.

of time. Two time-dependent wavenumber spectra are presented in fig. 13 together with the corresponding temporal power spectra of the intensity of each state taken at one point in the cell. Each line on the plots (fig. 13(a, b)) represents the power spectrum in k-space of the optical signal at one moment. The time interval between lines is $0.32t_v$. Both wavenumber spectra presented are from data measured at $\psi = -0.058$ with $\Gamma = 20$. The data used in fig. 13(a) were taken at $\epsilon = 0.0015$ where the state observed was a simple

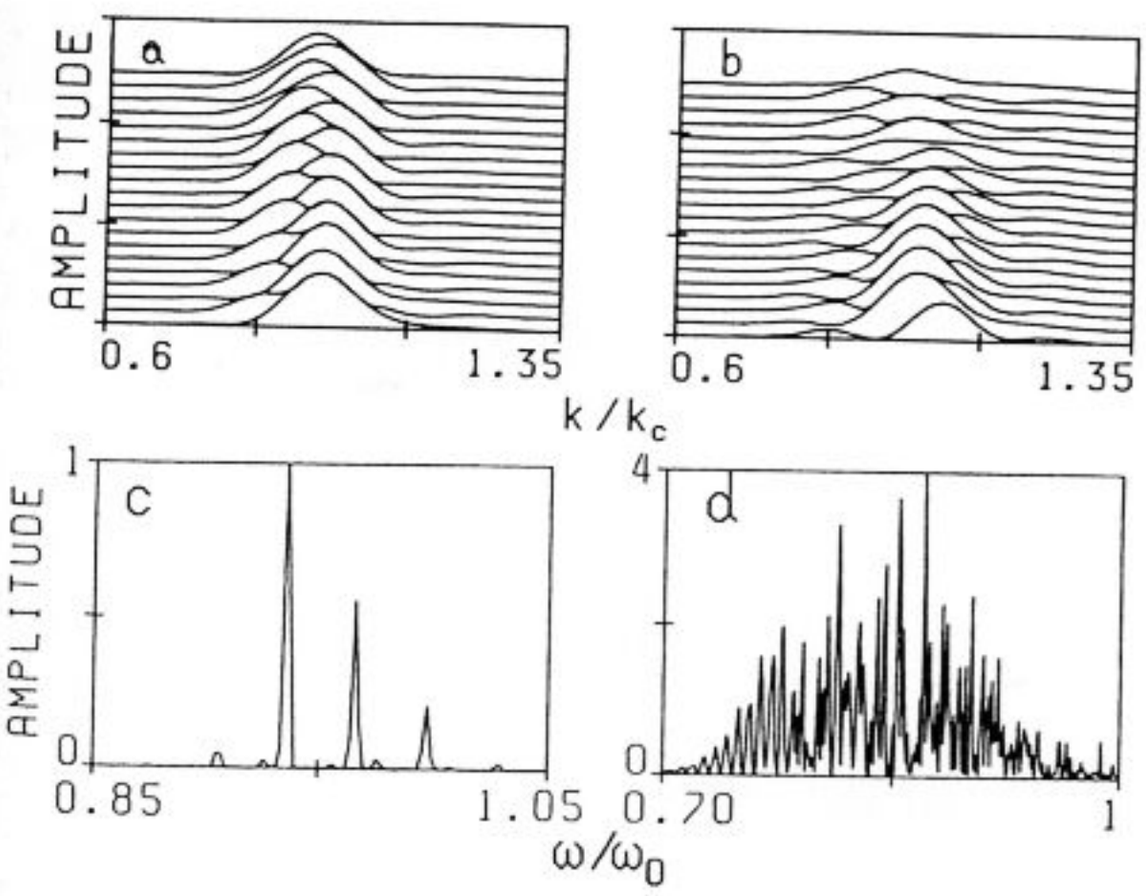

Fig. 13. Wavenumber spectra of blinking TW states at consecutive time intervals of $0.32t_v$, at $\epsilon = 1.5 \times 10^{-3}$ (a), and $\epsilon = 3 \times 10^{-3}$ (b) for $\psi = -0.058$. (c) and (d) are the temporal power spectra of a spatial point corresponding to (a) and (b) respectively.

2-frequency quasiperiodic state, as seen by its power spectrum in time (fig. 13(c)). The data used for fig. 13(b) were taken at $\epsilon = 0.003$ where the observed state corresponds to the more complicated blinking states which may be the predicted 3-frequency quasiperiodic or chaotic state described previously. The power spectrum in time of this state is presented in fig. 13(d). It is clearly seen that the wavenumber of the blinking state never settles down to a steady state value. At smaller values of ϵ the temporal modulation of the k-spectrum of the blinking state with a half period of TW is similar to the time-dependent k-spectra of the nonlinear CPW mentioned above, and can probably be partially ascribed to a linear mechanism. A possible explanation for the time dependence on the fast time scale is that these states correspond to a two-wavenumber state (two separate values of k). The simple spectra are similar to those obtained in simulations of a linear superposition of two CPW states with two wavenumbers differing by a value, Δk, obtained from the experimental spectrum. The results of this simulation using the function

$$A(x,t) = e^{\gamma x}\cos(kx - \omega t)\cos(\Delta kx - \Delta\omega t) + e^{-\gamma x}\cos(kx + \omega t)\sin(\Delta kx + \Delta\omega t) \quad (5)$$

are presented in fig. 14(a) where the spatio-temporal behavior of these states is shown. The corresponding wavenumber spectrum in time of this state is presented in fig. 14(b). The parameters, ω, k, $\Delta\omega$, and Δk used in eq. (5) are the same as for the experimental data presented in fig. 13(a, c). Although the linear model correctly describes temporal modulation on the fast time scale, it cannot explain the more complicated k-spectra of the blinking TW higher on the branch (fig. 13(b)). In order to emphasize this point we present additional data of the time-dependent k-spectra at $\psi = -0.058$ and $\epsilon = 3.4 \times 10^{-3}$ (fig. 15). Temporal modulation on the fast time scale is still evident here, but time dependence of k-spectra on the

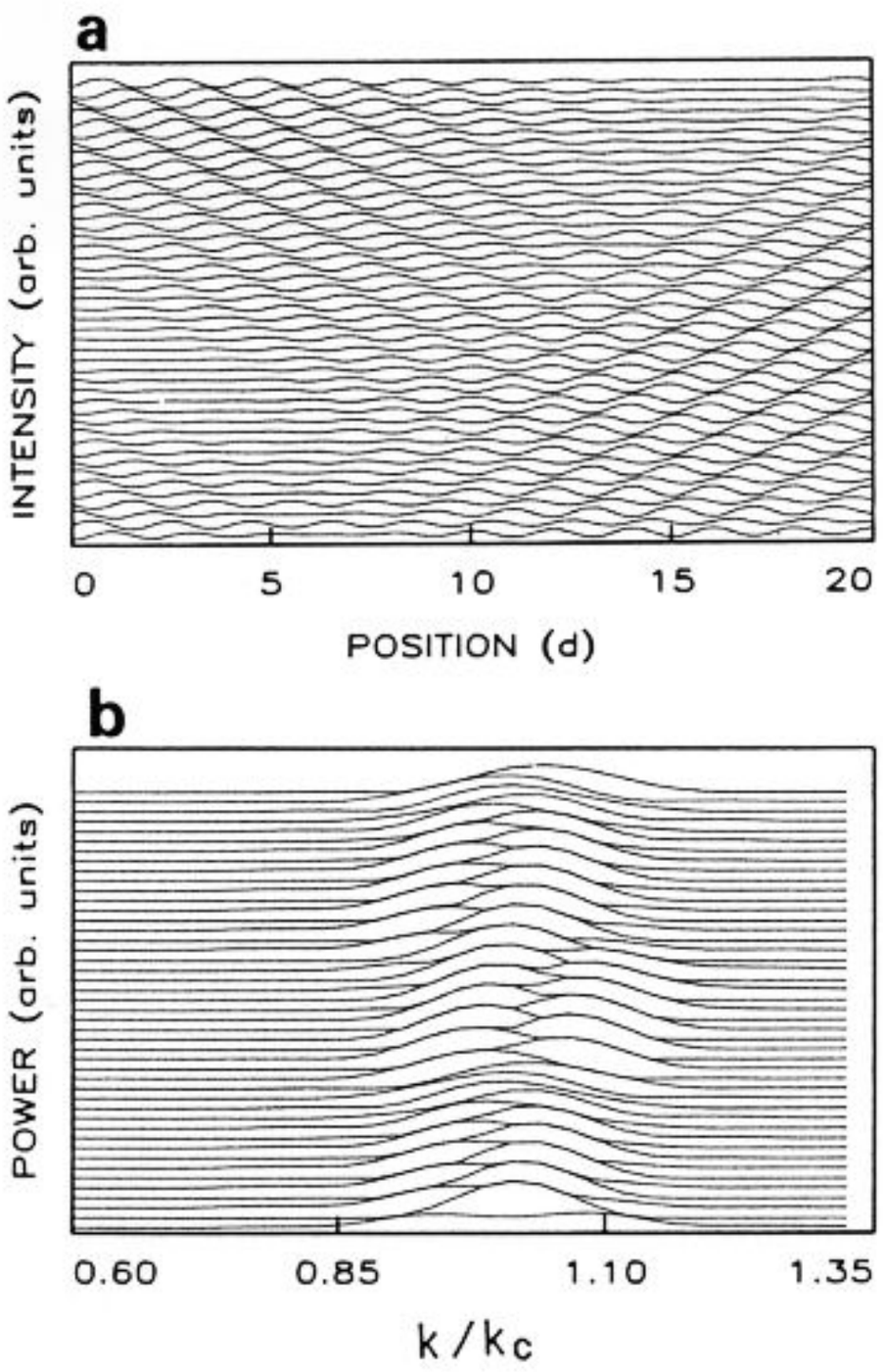

Fig. 14. (a) A contour plot of the simulated $2k$ state described by eq. (5). The parameters used were: $\gamma = 0.082$, $k = \pi$, $\Delta k = 0.035k$, $\omega = 2\pi/4.15$ and $\Delta\omega = \omega/k\,\Delta k$. (b) The spatial power spectrum in time of the simulated $2k$ state presented in (a).

long time scale cannot be explained by the model. The instability in the average wavenumber, the band of stable wavenumbers observed in the blinking TW which is wider than theoretically predicted stable, and complicated time dependence of k-spectra at higher ϵ suggest that the entire

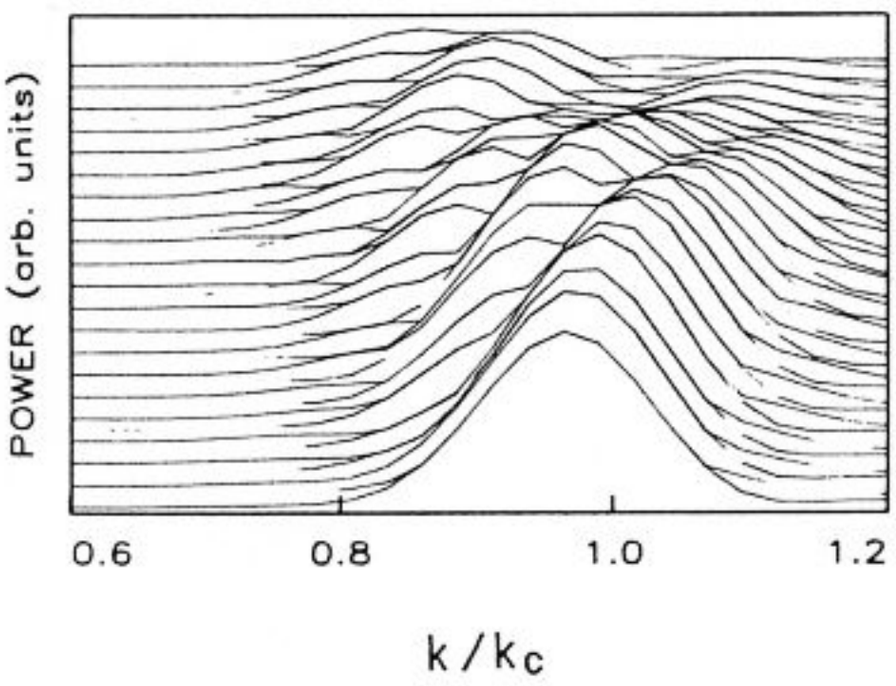

Fig. 15. Spatial power spectrum as a function of time of a blinking state observed for $\psi = -0.058$, $\Gamma = 20$, at $\epsilon = 3.4 \times 10^{-3}$ taken at $0.32t_v$ intervals in time.

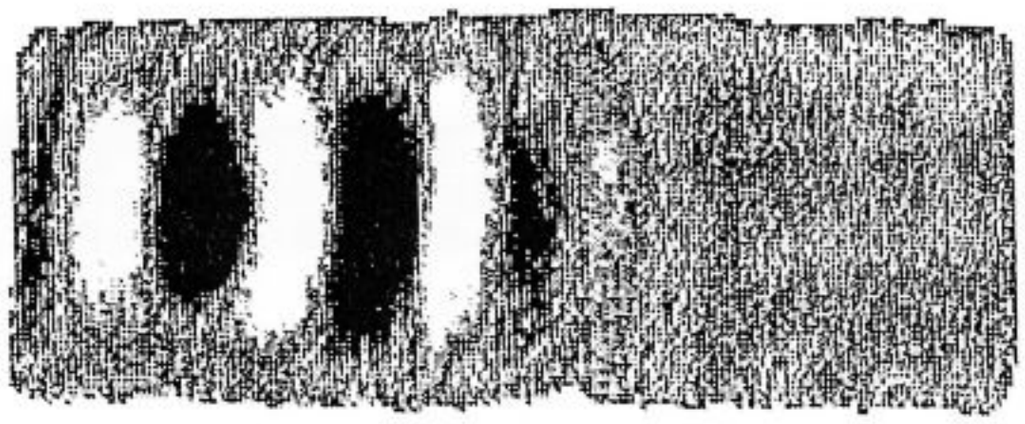

Fig. 16. Shadowgraph picture of a confined state for $\psi = -0.058$, $\Gamma = 12$ and $\epsilon = 0.0035$.

phenomena cannot be attributed to a linear mechanism. It is possible that the linear mechanism can drive TW toward instability. Then at higher ϵ the interplay between two nonlinear mechanisms may be responsible for more complicated behavior particularly on long time scales [40, 76]. One of them is the wavenumber selection behind a front at convectively unstable conditions (eq. (2)) [3]. This selected wavenumber k^* may become unstable to a modulational instability if k^* is selected outside of the stable wavenumber band [78]. As theoretical calculations show this may lead to time-dependent behavior in the k-spectrum [77].

3.1.3. *Confined TW state*

The confined branch can be reached by either a continuous transition from the blinking state or directly from the conduction state via the linear CPW. The nature of the confined state is illustrated in fig. 16 by a shadowgraph picture for $\epsilon = 0.0035$ and $\Gamma = 12$ at $\psi = -0.058$, and in fig. 17 we show the intensity of another confined TW state for a

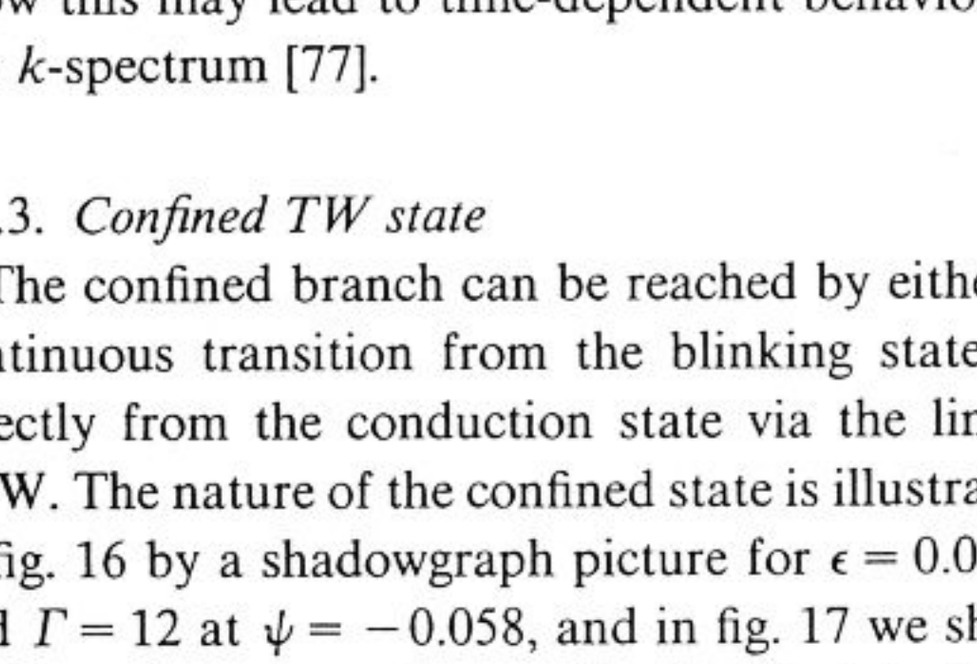

Fig. 17. Contour plot of a confined state observed for $\psi = -0.058$, $\Gamma = 20$, at $\epsilon = 0.017$.

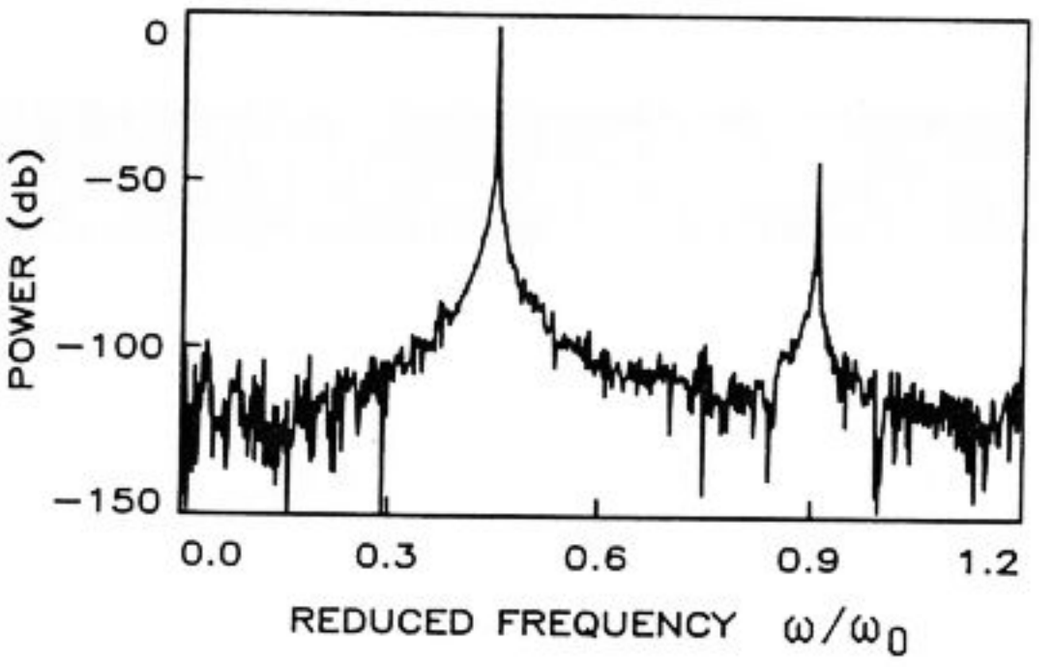

Fig. 18. The temporal power spectrum of a confined state observed for $\psi = -0.058$, $\Gamma = 12$, at $\epsilon = 0.0069$.

cell of aspect ratio 20 at $\epsilon = 0.017$ and $\psi = -0.058$ as a function of position in the cell. The TW are always observed to propagate in the direction of the cell walls while the state's envelope remains constant in time. A power spectrum of the shadowgraph signal taken at one point is presented in fig. 18. This consists of a single peak together with its 2nd harmonic. From this graph it is already clear that the frequency of the confined state differs considerably from the neutral frequency, i.e. the linear concentration profile should be distorted considerably. Fig. 19(b) presents the detailed studies of the frequency of the confined TW state at different lateral boundary conditions at $\psi = -0.058$ as a function of ΔT. The first conclusion is that the frequency of confined TW decreases linearly with ϵ. The second conclusion is that the frequencies along the confined branch for three sets of data are identical. (Data are presented for the cell with the low thermal conductivity polypropelene (PP) walls, medium thermal conductivity high density polyethylene (HDPE) walls and metal walls.) Moreover, we also checked that both heat transport and the region of existence of the confined branch were unaffected by variations of lateral boundary conditions or by changes in aspect ratio (fig. 19(a)). Since, as we already pointed out, the convective onset depends crucially on the aspect ratio, on boundary conditions and on the value of ψ, the confined TW branch only appears to be increasingly hysteretic if, the critical

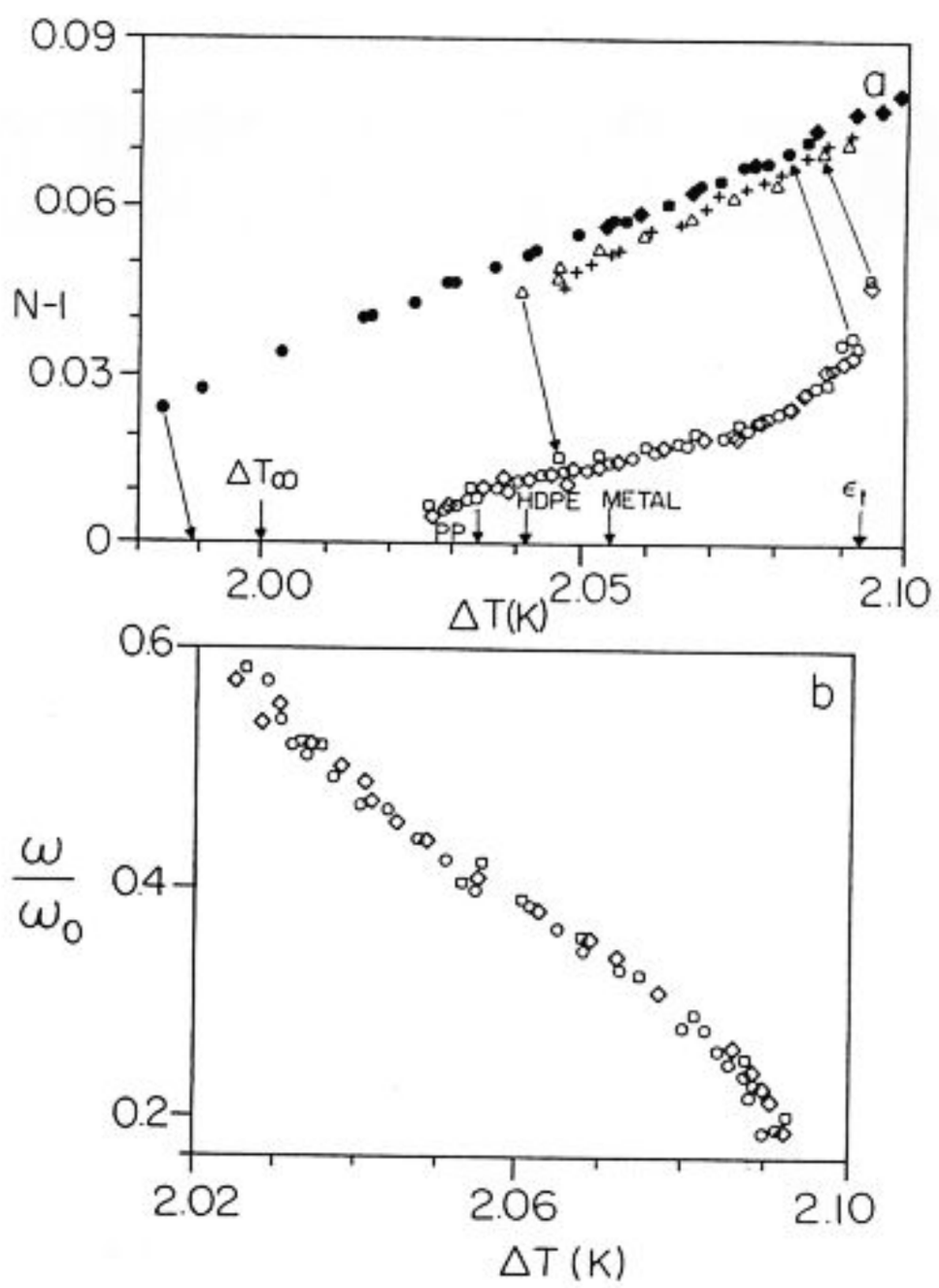

Fig. 19. (a) $N-1$ measurements as a function of ΔT for $\psi = -0.058$ for cells with different lateral walls (squares – PP, diamonds – HDPE, circles – metal walls, open symbols – confined TW, solid symbols – stationary convection, triangles – full TW for PP walls, crosses – full TW for HDPE walls. (b) Frequency ratio ω/ω_0 as a function of ϵ for confined TW at $\psi = -0.058$. $\omega_0 = 4.9$ is the neutral frequency.

threshold, $\Delta T_c(\text{exp})$, is shifted toward higher and higher temperature differences (see fig. 19(a)) due to the boundary conditions or aspect ratio variations. Thus the nonlinear behavior of the confined TW is independent of the location of the experimentally measured onset, $\Delta T_c(\text{exp})$. Third conclusion is that the transition from the confined TW branch to saturated TW which corresponds to the transition from convectively to absolutely unstable conditions, occurs at the same value of ϵ independent of the boundary conditions and of the cell length in agreement with the theoretical prediction [34, 35]. Quantitative verification of this important result of the theory was performed over a wide range of ψ between -0.005 and -0.078 and for various cell lengths and lateral boundary conditions [72]. The results are presented in fig. 20. The experimental value for s_t^* at which the transition occurs is independent of ψ as predicted

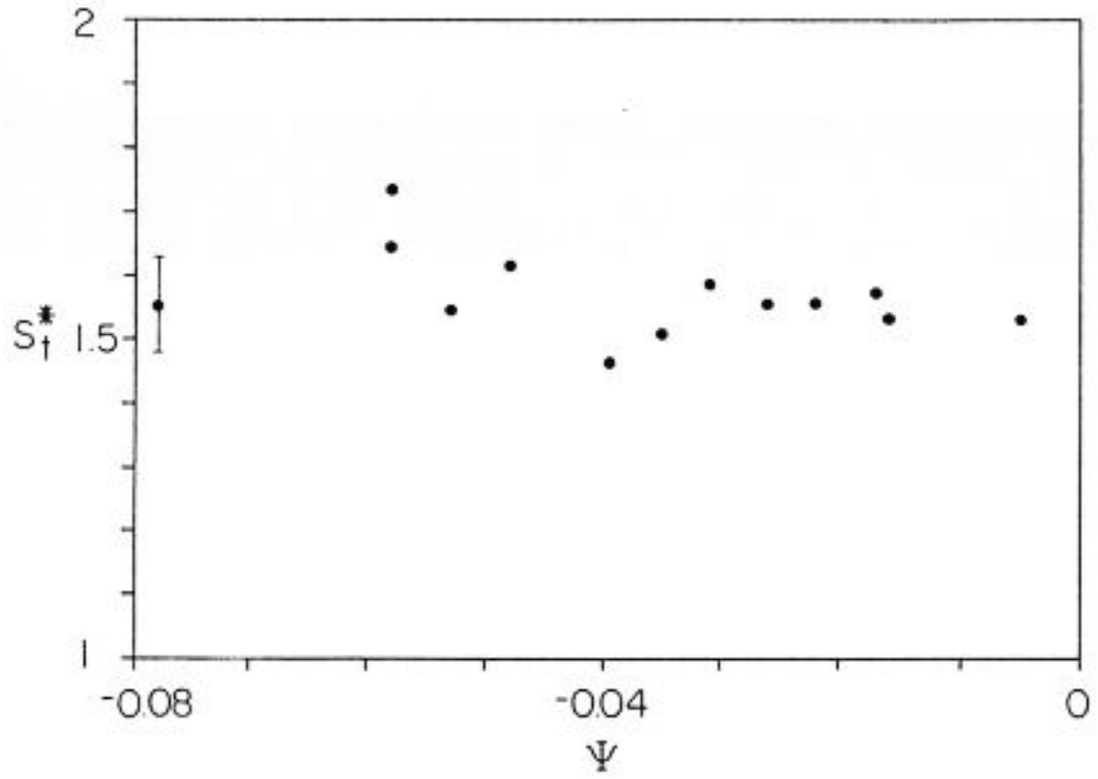

Fig. 20. Non-dimensional group velocity of TW at the transition from the confined branch to full TW, s_t^*, as a function of ψ. A typical error bar is shown.

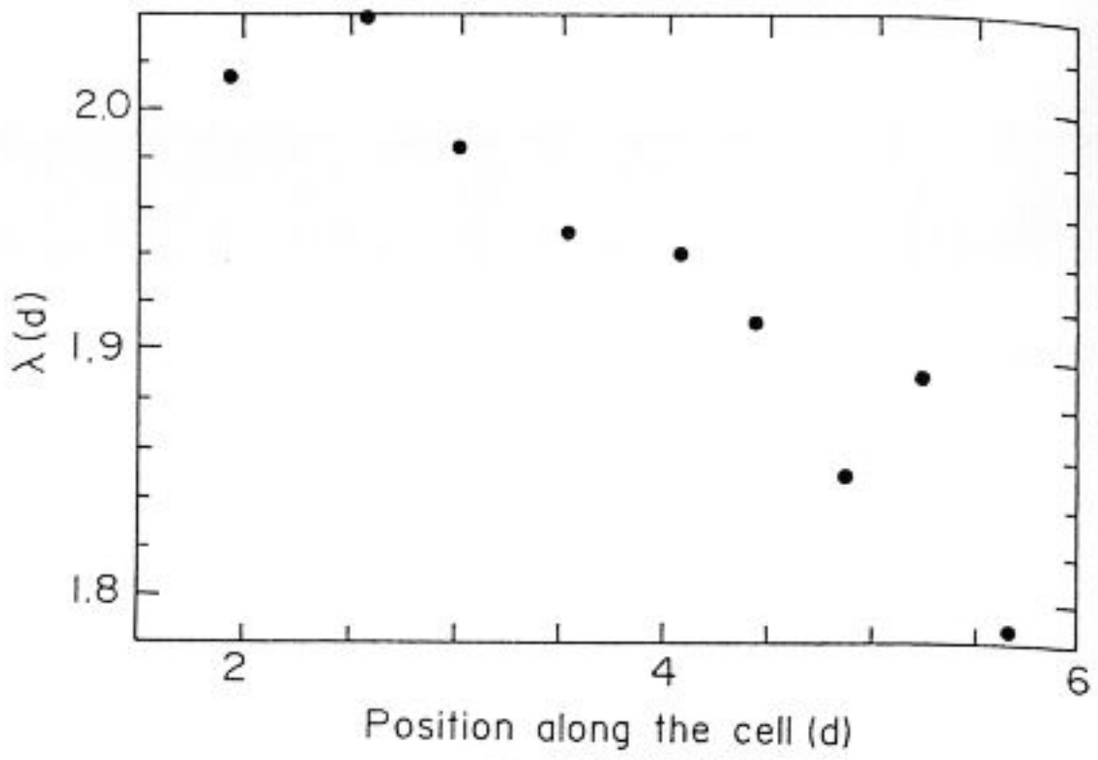

Fig. 21. The wavelength, λ, of a confined state as a function of the position along the cell. The data shown were taken for $\psi = -0.058$, $\Gamma = 20$, and $\epsilon = 0.015$.

and is equal to 1.57 ± 0.07. Since the observed bifurcation to oscillatory convection is subcritical unlike the supercritical one considered by the theory [34], one cannot expect exact quantitative agreement with the predicted value or s_t^* but the existence of a sharp selection criterion is indeed apparent.

Another possible consequence of the convective instability condition is the experimentally observed wavenumber selection on the confined TW branch. Since the confined state is considered as a front-type solution of the amplitude equation, one could expect to see evidence of wavenumber selection as a function of ϵ along the branch [51, 79–84]. It is known that this is one of the characteristic features of the front-like solution. Theoretical calculations for GGL equation gives the selected wavenumber determined by eq. (2).

First we note that the observed wavenumber, k, for a particular value of ϵ is not constant along the length of the cell. This is illustrated in fig. 21 where we show the wavelength, λ, as a function of the position along the cell. The dependence of λ on the cell position presented in the figure is fairly typical for any confined state we observed, and is independent of the exact value of ψ or ϵ. This behavior is also seen for cells of aspect ratios $\Gamma = 12$ and $\Gamma = 20$. In general we find that k becomes larger as one moves away from the end of the cell. There is a fairly continuous change in the wavenumber, as observed in the figure, and the total change in the wavenumber throughout the cell is on the order of 10%. This situation is similar to results of numerical simulations performed by Dee and Langer [79] with the Swift–Hohenberg equation for the case of a moving vortex front propagating into an unstable conduction state. The authors observed a jump to a value of k that was about 10% higher than the value selected in the bulk after the front was past. Similar observations were made experimentally in the vortex-front propagation experiment [51], but in both cases the wavenumber of the state immediately behind the front was fairly constant. It is conceivable that the increase of the wavelength near the wall is an effect due to the boundaries.

In order to verify wavenumber selection we used an average wavelength calculated by averaging over the rolls in the central region of the confined state. The validity of this procedure was checked by comparing plots such as those shown in fig. 21 for different values of ϵ. It was found that the entire plot was, in general, shifted as a function of ϵ so that the "stretching" or "compression" of the wavenumbers observed at the state's ends apparently depends only on the average wavenumber of the state and is not ϵ dependent. The results of this analysis for a cell of

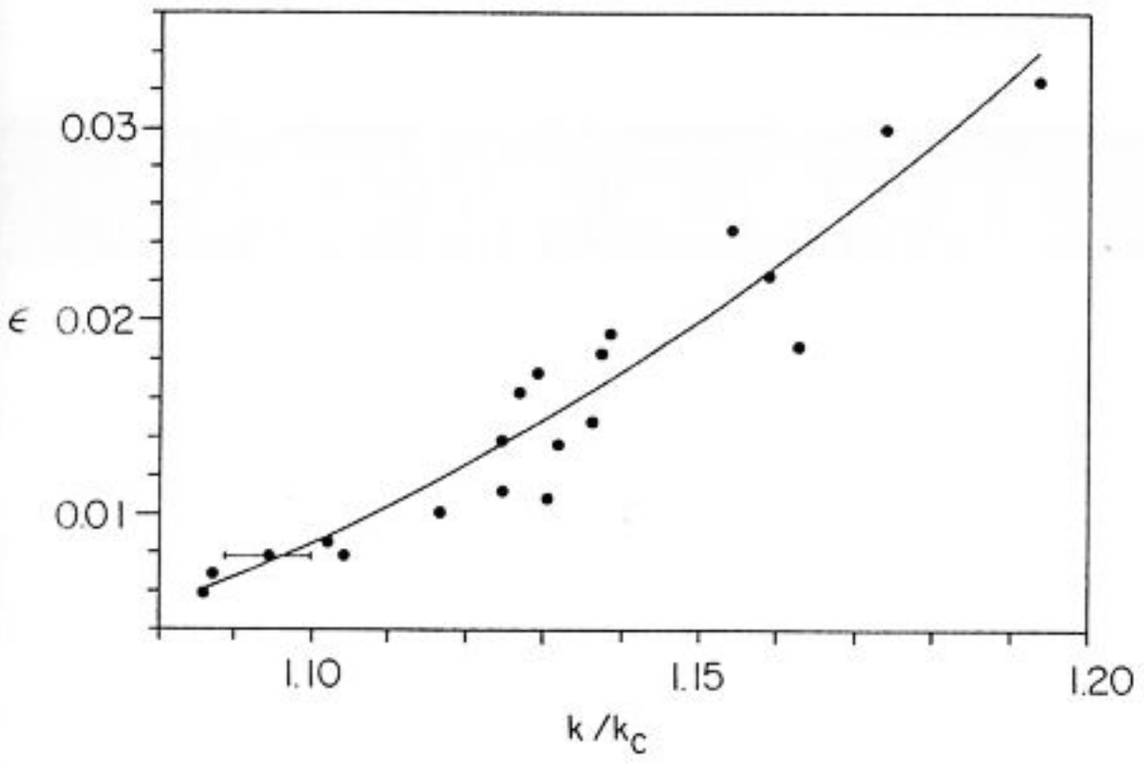

Fig. 22. Dependence of average k/k_c as a function of ϵ at $\psi = -0.058$, $\Gamma = 20$, and $\epsilon = 0.015$.

aspect ratio $\Gamma = 20$ at $\psi = -0.058$ are shown in fig. 22. The solid line in the figure is the fit of the data to $\bar{k}/k_c - 1 = (0.405 \pm 0.03)\epsilon^{1/2}\xi_0^{-1}$ ($k_c = 2.98 \pm 0.04$ is the critical value of the wavenumber obtained from the fit). The fit should be compared with an expression $k/k_c - 1 = 0.28\epsilon^{1/2}\xi_0^{-1}$ obtained from eq. (2) using $c_2 = -5.6$ (from ref. [85]) and $c_1 = -0.049$ (from ref. [60]). We do not find quantitative agreement between the observed wavenumbers selection and the theoretical prediction, although eq. (2) predicts the observed ϵ dependence.

An interesting point concerns the value of the critical wavenumber obtained from the fit. Linear stability analysis predicts at $\psi = -0.058$, $k_c = 3.11$ (ref. [60]) which is in good agreement with the experimental value of k_c for the linear and the nonlinear CPW ($k_c = 3.09$). The average wavenumber obtained in the blinking state of $\psi = -0.058$ lies in the range between 2.90 and 2.98 which is consistent with the result for the critical wavenumber obtained from the fit for the confined TW branch which follows the blinking states. Thus changes in TW patterns are accompanied by changes in the average wavenumber, first by a decrease of about $0.07k_c$ (from CPW to blinking TW), and then by an increase of about $0.05k_c$ (from blinking to confined TW), and finally by continuous growth with ϵ (about 10%) along the confined branch. We also find that the average wavenumber of the confined state transcends the

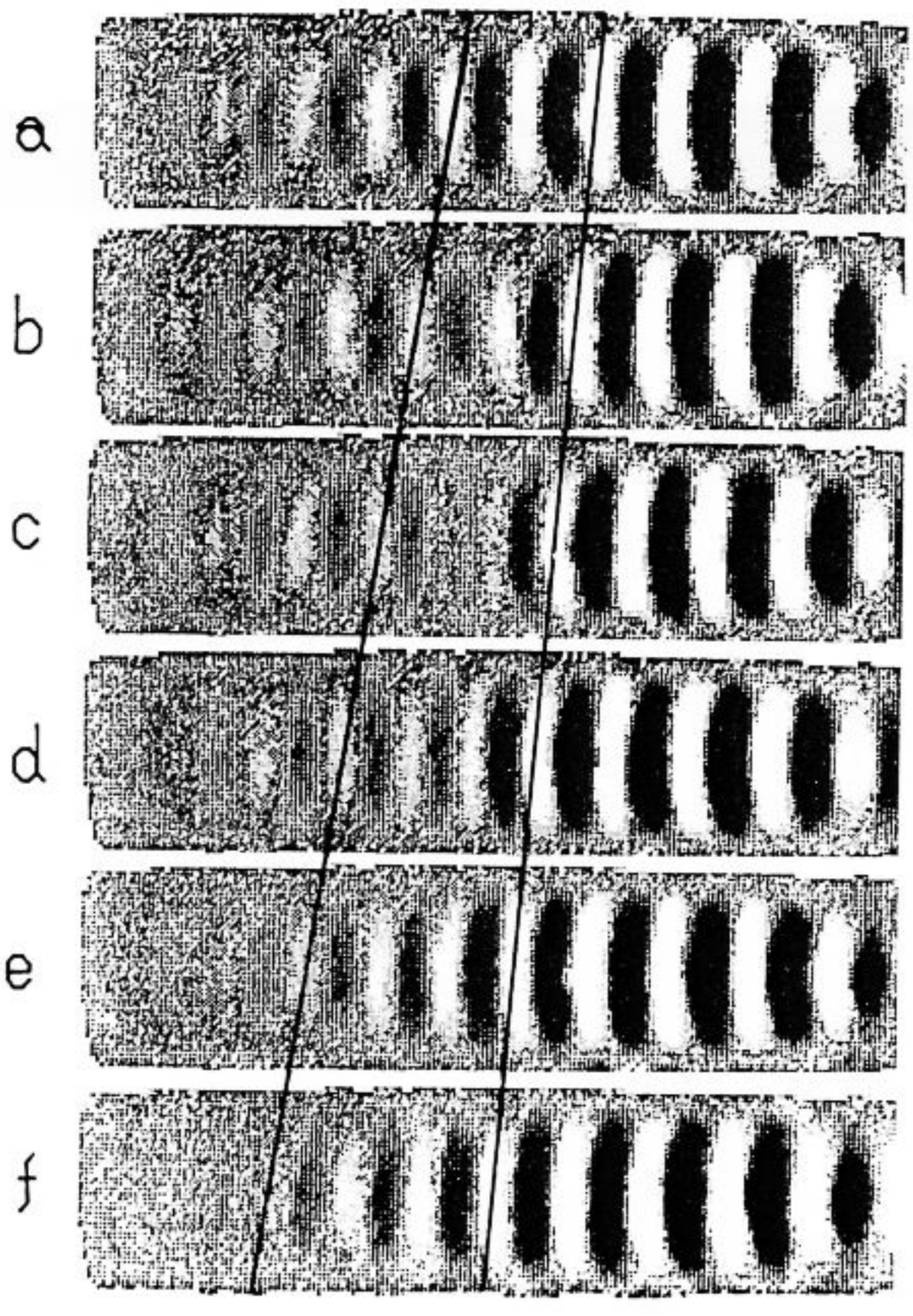

Fig. 23. Series of shadowgraph pictures depicting the two-frequency $2 - k$ state observed for large Γ and relatively high ϵ. Here $\Gamma = 20$, $\psi = -0.058$, and $\epsilon = 0.028$. Lines are drawn along TW crests to demonstrate the two different TW velocities in evidence.

modulationally unstable band of states [78] for relatively large values of ϵ that might lead to instability of the state. For a large aspect ratio cell we find that the simple confined state described above becomes unstable at ϵ on the order of 0.01–0.04 depending on ψ.

A sequence of shadowgraph pictures of the new state with a time interval of $0.64t_v$ between pictures is presented in fig. 23. (This state is at $\psi = -0.58$ for a cell with $\Gamma = 20$ and $\epsilon = 0.028$.) One can see that this new state consists of two separate confined states. Each of these confined states is made up of TW traveling in the same direction but with separate frequencies. The TW nearest the wall appears to be a direct continuation

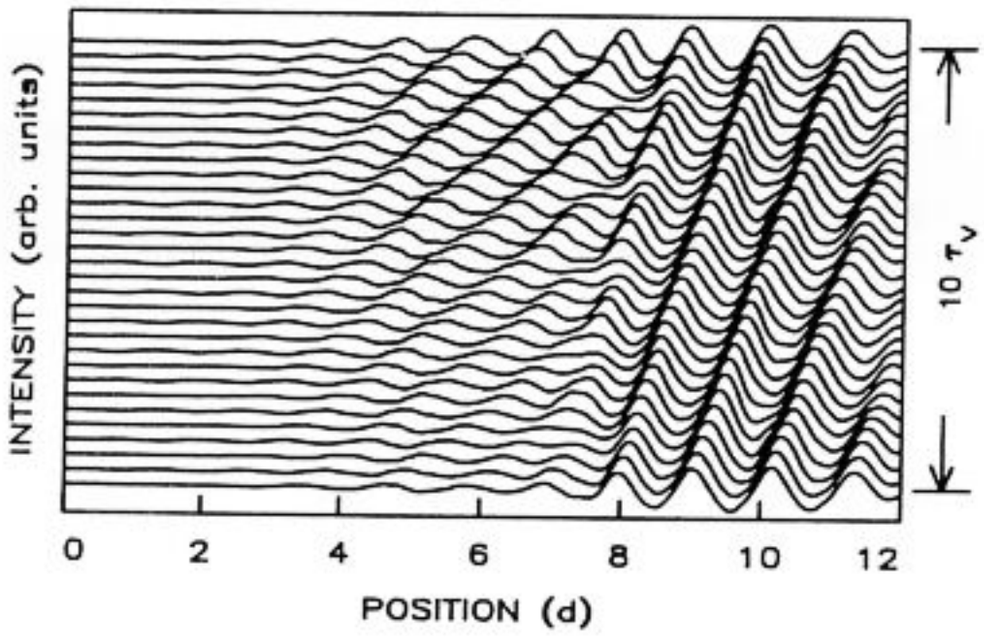

Fig. 24. A contour plot of two-frequency $2-k$ state for $\psi = -0.058$, $\Gamma = 20$, and $\epsilon = 0.032$. Defect formation at the meeting place of the two confined states is seen.

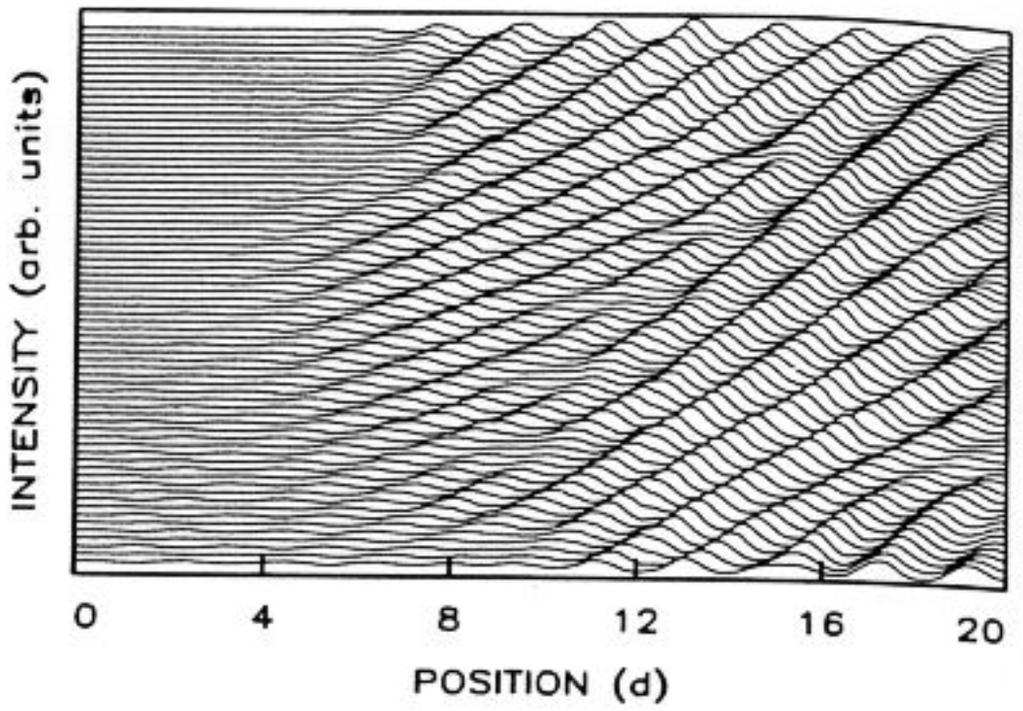

Fig. 25. Contour plot of a 2-frequency state for $\omega = -0.058$, $\Gamma = 20$, and $\epsilon = 0.027$. 70 lines are shown with an interval of $0.32t_v$ between lines. The defect between states of different frequency can be seen to be migrating to the right of the cell.

of the original, simple TW branch seen for lower values of ϵ. The frequency of this slower state evolves continuously from that of the simple confined states lower on the branch. On the other hand, the TW frequency of the faster moving state appears unconnected to that of the other slower moving part and is moving approximately at the neutral frequency. In fact, at some moments (transient) CPW can be seen that have formed in the part of the cell not occupied by the slower TW. The two separate TW frequencies are highlighted on the figure by two lines that follow the propagating crest of a roll on the left of the cell as well as a roll on the right of the cell. The difference in the TW velocity of the two sides can be seen by the difference in the slopes of the two lines. A more detailed view of the dynamics of this state can be seen in fig. 24 which shows a contour plot of a two-frequency state when the time between lines in the figure is $0.32t_v$. (This plot was taken at the same values of ψ and Γ as in fig. 23 for $\epsilon = 0.032$.) The two separate frequencies in the state can be seen clearly as can the creation of a defect at the meeting place of the two states. This defect is formed as a result of the faster state to the left of the figure, 'outrunning' the slower TW state to the right. The defect is formed when the roll, caught between the two states, is squeezed until it becomes unstable. At this stage, the roll simply disappears in a discontinuous way and a new, longer wavelength roll is formed at the intersection. This process then repeats itself. The formation and annihilation of such a defect can be seen in the picture sequence in fig. 23. The faster moving component of the state is not generally stable and, for a fixed value of heat flux to the cell will, appear and disappear in time. The slower moving TW state always remains in the cell. Another view of this behavior is presented in fig. 25 for $\epsilon = 0.027$. In this figure we present a contour plot of 70 consecutive lines taken at time intervals of $0.32t_v$. We see the long time dynamics of the defect that separates the fast and slow TW that comprise the state. At the bottom of the figure on the far side of the cell, we see the formation of the higher frequency state where evidence of the formation of a CPW state can be seen. The interface between this and the slower state eventually forms a defect which then is seen to propagate through the slower state to the right, finally leaving the cell. Approximately at that point the higher frequency state disappears. The state formed at the top of the picture is not stable and will eventually evolve to a confined state which takes up only about half of the cell. At this point the scenario described in the figure will repeat itself.

Some knowledge of the dynamics of the two states shown in fig. 25 is gained by looking at the corresponding spatial spectrum as it evolves in

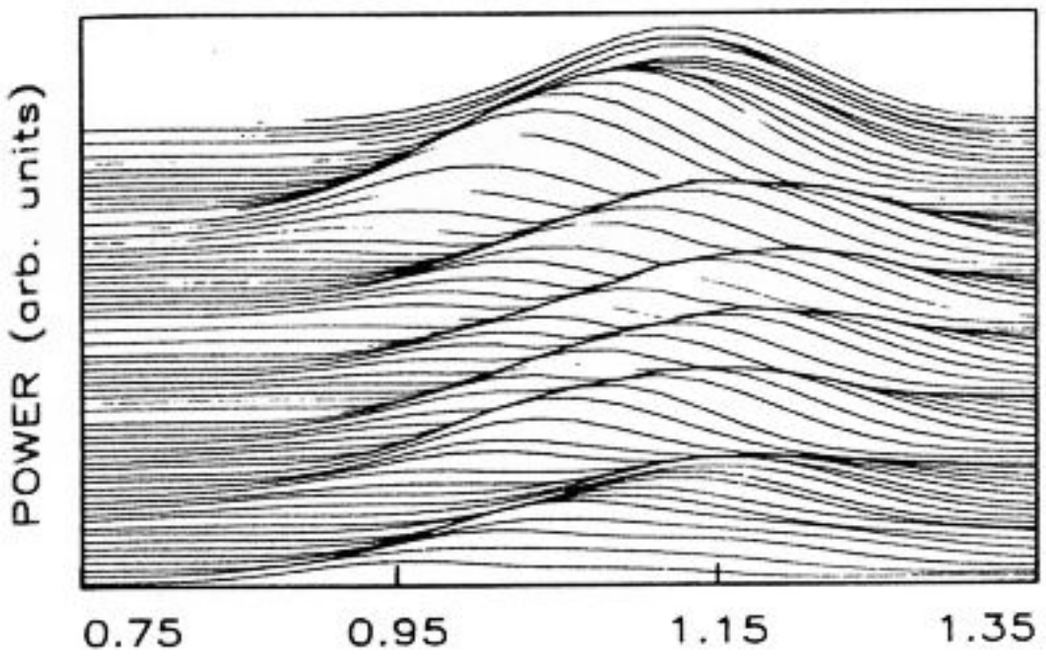

Fig. 26. Spatial power spectra of the data shown in fig. 25. The wavenumber is seen to increase until the formation of a defect. At that point the wavenumber is decreased discontinuously.

time. This is presented in fig. 26. In the figure, one can observe a continuously increasing of the average wavenumber of the state as a function of time corresponding to a compression of the entire state. This compression continues until a defect is formed (a roll pair is lost) at which point the entire spectrum discontinuously jumps back to a lower value of k. At the top of the figure, the spectrum is seen to settle down as the faster state disappears from the system.

States very similar to those described above have been observed in numerical simulations of a single complex Ginzburg–Landau equation by Nozaki and Bekki in ref. [3]. They explained their observations as resulting from the competition between the selection of an initial wavenumber by way of a front propagation mechanism which is in evidence at the border between the faster propagating state and the quiescent (conduction) state. This selected wavenumber, although linearly stable, can be outside of the band of modulationally stable wavenumbers [78]. In this case, a different wavelength is chosen by the higher amplitude state found downstream from the original front. In their simulations, these authors found that instead of the entire state choosing one single wavenumber, a front separating two states having different wavenumbers and frequencies is formed. This new state can be stable or lead to chaotic behavior. This depends on both k and the coefficients of the amplitude equation. This scenario may indeed be relevant to our experimental observations since a clear difference in wavenumber is also experimentally observed between the higher and lower frequency states. The difference in the wavenumbers between the higher and lower frequency TW is on the order of 5–10%. (The higher wavenumber corresponds to the state with the higher frequency.) These states very much resemble similar states observed in recent experiments conducted in an annular cell [86].

Recently, the motion and stability of slowly varying wavetrains described by GGL equation were investigated theoretically [87]. It was shown that their dynamics should be governed by a simple nonlinear wave (Burgers') equation which can develop shocks corresponding to rapid changes in wavenumber. The Burgers' equation is in fact a nonlinear phase diffusion equation. This equation allows the development of strong shocks in a diffusively unstable case in regions where there is a rapid transition between two wavenumbers differing by an order of unity. The equation also allows the development of weak shocks in the diffusively stable case. This shock has a width on the order of $1/\Delta k$, where Δk is a difference between wavenumbers on both sides of the front, and it moves with a speed $c = \Delta\omega/\Delta k$. The defects, observed between fast and slow confined TW states, are probably related to the weak shock. In other words, basically it is a rigorous way to describe dynamics of the modulational instability of the nonlinear TW. In the next section we will consider an analogous approach to describe the transition to spatio-temporal complex behavior in anisotropic systems.

Finally, we would like to emphasize once more the importance of preserving the one-dimensional geometry of the cell in order to observe the simple scenario and patterns presented above. The only three-dimensional effects observed were a slight

curvature of the convection rolls that was symmetric about an axis along the propagation direction. The scenario described here for one-dimensional systems changes drastically, both quantitatively and qualitatively, when the aspect ratio along the width of the cell is increased. Even a variation in the width from $4d$ to $5d$ leads to three-dimensional effects which manifest themselves in a vast variety of three-dimensional patterns observed (part of them even classified in ref. [88]). As we studied and reported earlier [37], even highly nonlinear states remain two-dimensional if the cell width is kept small in contrast to the conclusion reached in ref. [88]. It is feasible that more complicated spatio-temporal behavior reported in ref. [88] is the result of deviations from the one-dimensional geometry of the cell. Particularly, as suggested in ref. [88], aspect ratio dependence of s_t^* (which was checked only for one value of ψ) accompanies the appearance of various TW patterns before the transition. Moreover, the transition occurs to the state which consists of steady rolls [88] and is not the saturated TW as considered by the theory [34, 35]. Therefore, relevance of this observation [88] to the theoretical predictions [34, 35] is not clear.

3.2. *Defect-initiated turbulence in electroconvecting nematics*

Despite several experimental observations in convecting binary mixtures which indicate that instability may be responsible for complex dynamical behavior, we do not presently have convincing evidence of it. At the same time a uniform TW state discovered recently [47] in a very thin layer (about 15 μm thick) of electroconvecting nematics exhibits a simple scenario for the transition to spatio-temporal incoherent behavior through the nucleation of topological defects (dislocations) while the control parameter ϵ increases (here $\epsilon = V/V_c - 1$, and V_c is the critical voltage of the electroconvective onset). We would like to emphasize that we have not yet obtained quantitative verification of the BF instability theory (which, in fact, still does not exist in a complete form). The specific features of the transition, of the chaotic state itself and spatial and temporal dynamics of the scenario are, however, qualitatively described remarkably well by the theory [50]. This defect-initiated turbulent regime called "topological turbulence" was studied numerically by the GGL equation for an anisotropic flow [48–50].

According to the theory [49] there is a fundamental difference between one-dimensional and two-dimensional systems in their transition to turbulence. In one-dimensional systems in case of BF instability conditions (or diffusively unstable conditions) the number of unstable amplitude modes progressively increases. This means that the dynamics can be described just by the full GGL equation, and cannot be reduced to a phase equation. In two dimensions, the existence of localized amplitude modes (stable topological defects) allows for a nucleation transition [48–50]. Then chaotic dynamics of the phase field in a phase unstable region (at small value of the criterion which characterizes BF instability) [89] acts as a noise generator which initiates the creation of topological defects. Such a spatio-temporal state is called topological turbulence [49].

We studied the onset of spatio-temporal chaos which occurs in a uniform TW state. In the middle of the TW regime the waves are stable up to $\epsilon = 0.078$ (fig. 27). The regularity of the motion ceases above this value as indicated by the decay of the structure functions [47]. This destruction of spatio-temporal order stems from the creation of pairs of topological defects. Increasing the voltage increases the nucleation rate of defects and their total number. Once created the defects move through the system before annihilating in pairs. The disordered TW pattern is characterized by the presence and interaction of a large number of the moving dislocations. The scenario is illustrated in fig. 27. Three sets of pictures from a fixed square window containing about 20 rolls (i.e. a small fraction of the cell containing about 2000 rolls) are shown for 3 values of ϵ. At $\epsilon = 0.05$ (two

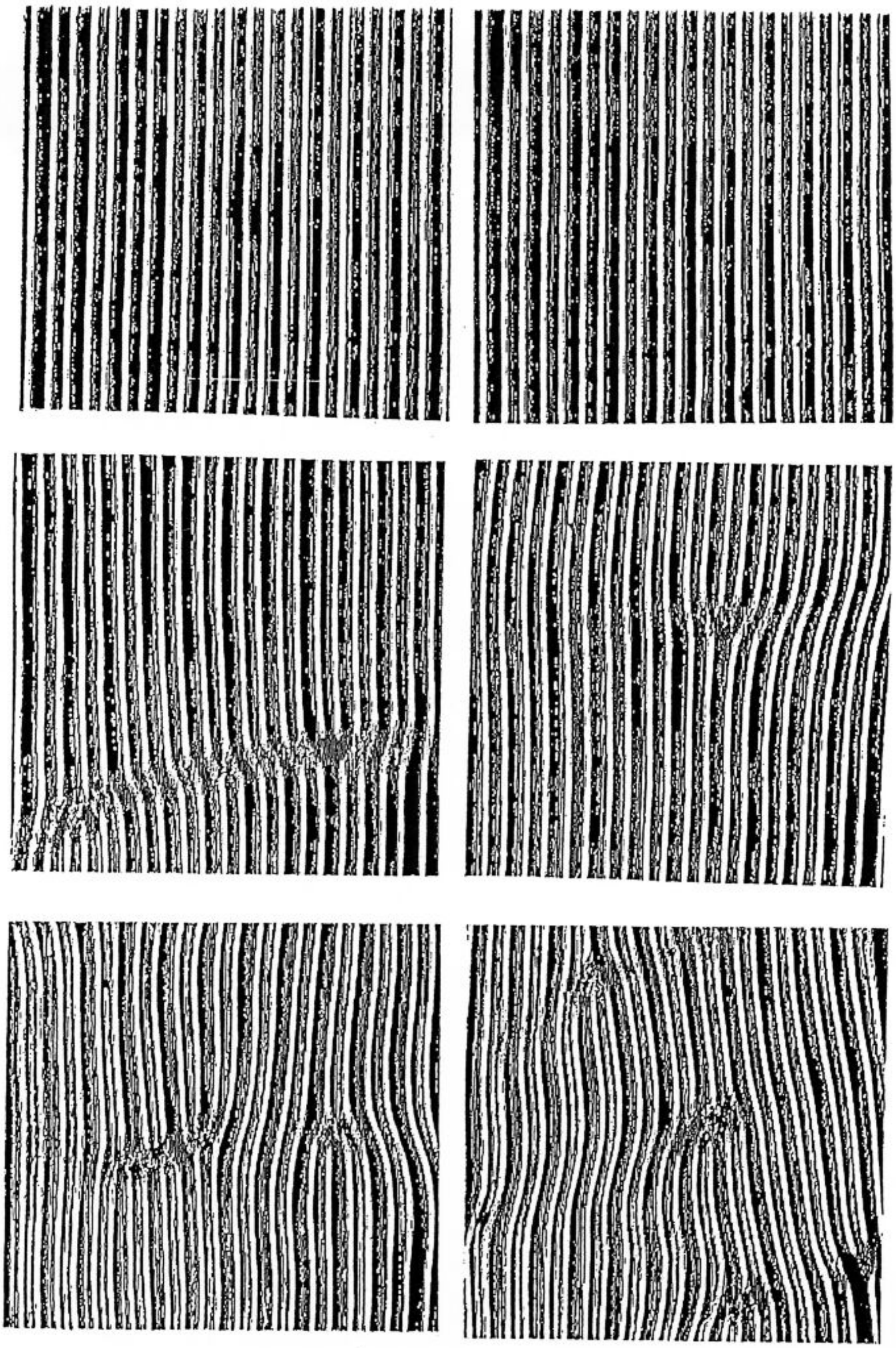

Fig. 27. Two images of the convection structure obtained at different times at $\epsilon = 0.05$ (upper two), $\epsilon = 0.10$ (middle) and $\epsilon = 0.17$ (lower two).

upper figures) defects were never observed. At $\epsilon = 0.1$ (two middle figures) the mean value of defects is about 2. The left figure shows a pair just created. The right figure shows the deformation field of a single defect. The asymmetry of that field indicates that it travels from right to left. The two lower figures show examples at $\epsilon = 0.17$, where the mean number of defects is about 4.

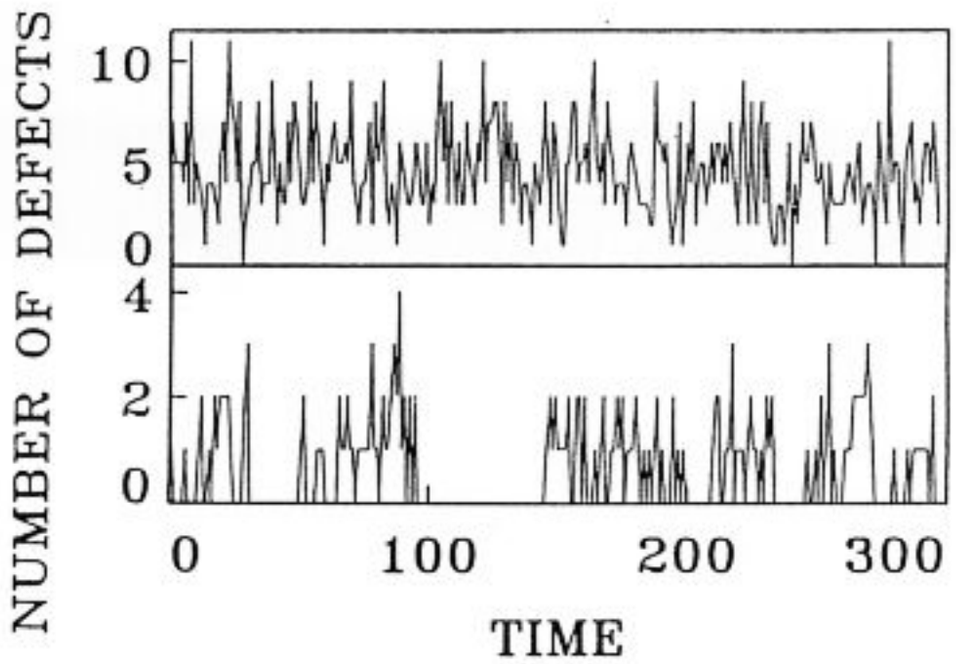

Fig. 28. Number of defects as a function of time for $\epsilon = 0.085$ (lower) and $\epsilon = 0.19$ (upper curve).

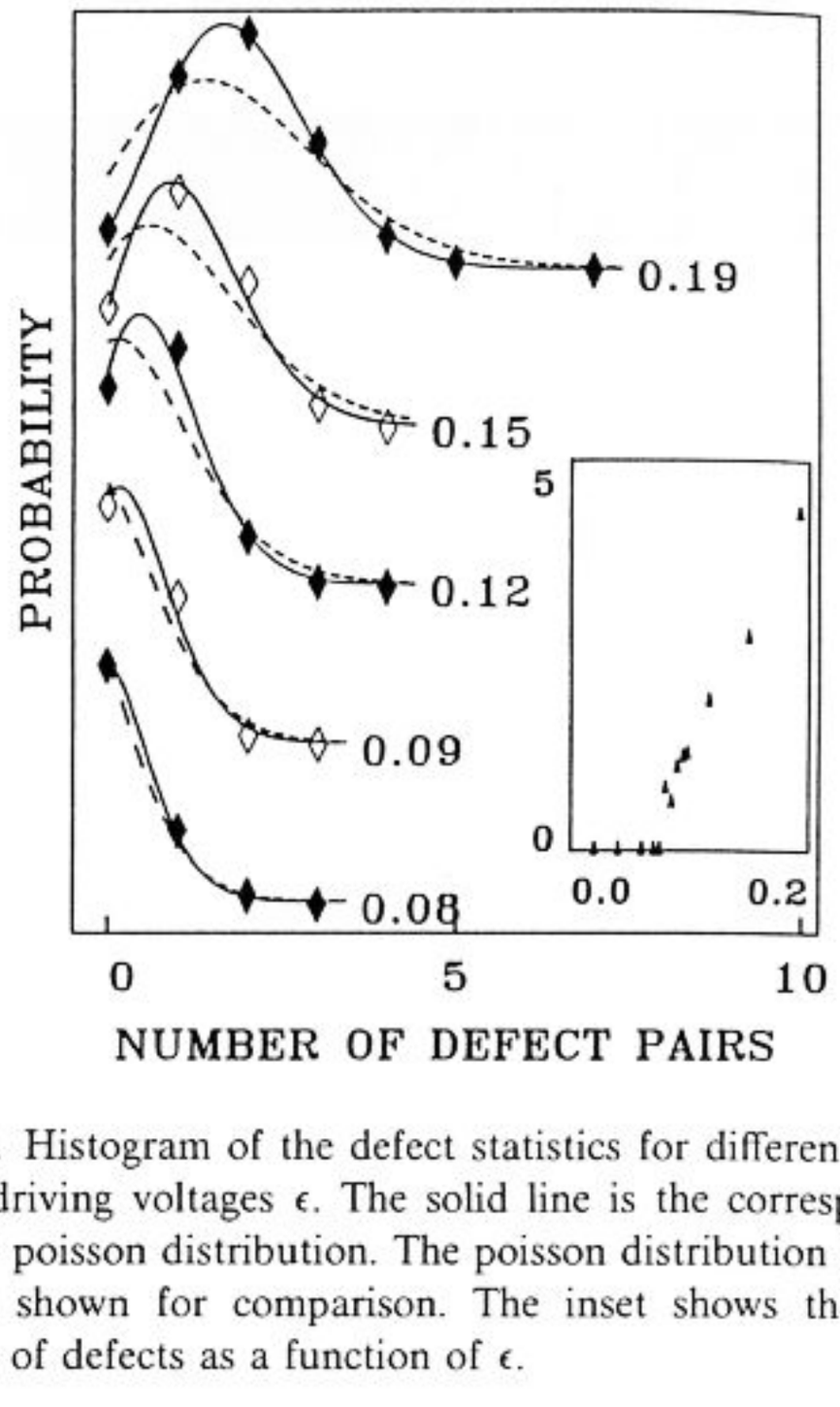

Fig. 29. Histogram of the defect statistics for different values of the driving voltages ϵ. The solid line is the corresponding squared poisson distribution. The poisson distribution (dashed line) is shown for comparison. The inset shows the mean number of defects as a function of ϵ.

We have counted the number of defects as a function of time for different values of ϵ. Two examples are shown in fig. 28. The lower curve, measured at $\epsilon = 0.085$, if very close to the onset of defects, is reminiscent of the intermittent data presented in fig. 4 of ref. [48]. The upper curve ($\epsilon = 0.19$), similar to fig. 1 of ref. [90], justifies the idea of a statistical description. A theory about the statistics of defects was presented recently [90] based on the idea that the probability to create a defect pair is given by ϵ, while the probability to annihilate a pair is proportional to the density of the defects squared. These mechanisms lead to a squared poisson distribution [90].

The histograms (diamonds) based on counting defects in about 400 pictures for different values of ϵ are shown in fig. 29. Eight hundred pictures were analysed for $\epsilon = 0.19$ to reduce the statistical errors. The agreement with the theoretical curve (solid line) is very good.

4. Discussions

We presented in this paper experimental results which basically can be understood qualitative and, in some aspects quantitatively, by using GGL equations which take into account effects of pattern translation and modulational instability of TW.

We reported on a sequence of TW patterns and their spatio-temporal behavior, observed as ϵ increases, in convecting binary mixtures in one-dimensional cells. Although the theory describes a supercritical bifurcation [34, 35] unlike the subcritical one studied experimentally [36–41], the theory gives a remarkably precise and qualitative picture of spatio-temporal behavior of TW. Besides asymmetric CPW which we did not observe, probably due to lack of resolution, all other independently predicted TW patterns were reproduced experimentally. Moreover, we verified experimentally the criterion of the transition from convectively to absolutely unstable conditions that shows up as transitions in observed TW patterns. This transition which does not depend on the value of ψ, lateral boundary conditions, and the length of the cell, occurs at a smaller value of s^* than expected by the theory [34], probably owing to the subcritical nature of the experimental bifurcation. Two

basic nonlinear TW states which we studied (CPW and blinking) exhibit frequencies which are close to the neutral frequency of the linear TW. Since it was suggested that perturbation of the linear concentration profile is directly related to this deviation, one expects that these states can be described by a perturbative theory. The third nonlinear state, confined TW, shows a frequency 2–3 times less than the neutral one. The theory however adequately describes its dynamics, including the transition from this state to strongly nonlinear saturated TW. We therefore concluded that the confined TW is a weakly nonlinear state. We found that the confined TW is independent of lateral boundary conditions unlike two other preceding weakly nonlinear states. This effect produces the unusual situation that the hysteretic region of confined TW depends on geometry and boundary conditions and may be extremely large (almost on the order of the existence of the state) while the hystereticregions of the nonlinear CPW and the blinking TW are unusually small. Further theoretical description of these aspects is desirable. In fig. 30 we present a summary of regions of weakly nonlinear TW states observed as a function of ψ. One can see from the data that, as already shown, only s_t^* appears to be independent of ψ. The region of existence of the confined TW increases for decreasing value of ψ. There is no further selection mechanism in s^* from the confined state to the blinking TW or CPW states. As we emphasized the region of existence of the blinking TW and nonlinear CPW depends on ψ, on the cell length, and on the boundary conditions. Since we present data for different cells all these factors were changed. The same is true for the convective onset. The largest experimental values of s^* were attained for values of ψ where blinking TW and CPW states were observed.

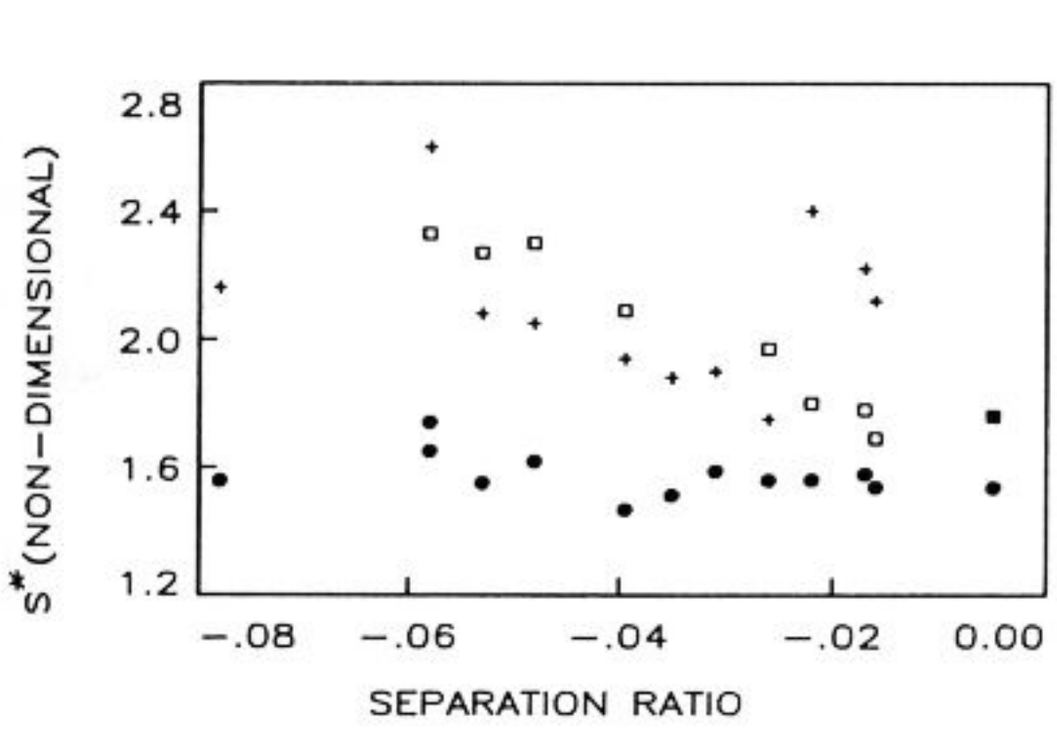

Fig. 30. The region of s^* observed experimentally. (circles) s^* where the confined TW loses stability (s_t^*) to the full TW branch; (squares) values of s^* where the confined branch loses stability to either conduction or to the blinking state; (crosses) values of s^* corresponding to $\Delta T_{c(exp)}$. Weakly nonlinear states were observed when these points went above the points represented by the squares.

Thus we confirm experimentally that in a finite one-dimensional geometry cell the convective nature of TW instability leads to very elaborate spatio-temporal pattern behavior. We also present, however, several observations which cannot be explained by the simple effect of pattern translation. We suggested that the long term temporal modulation of wavenumber spectra of blinking TW and shock-like patterns in the confined TW can be related to the modulational instability of TW.

Much stronger evidence for the manifestation of the BF instability has been presented in the case of TW in nematics. Numerical simulations of the GGL equation for an anisotropic flow [50] show spatio-temporal pattern behavior strikingly similar to the experimental results presented here. Further studies are necessary to make this comparison quantitative.

5. Summary

We have presented experimental results on spatio-temporal pattern behavior of nonlinear TW in two experimental systems. Experiments on convecting binary mixtures in one-dimensional geometry cells were devoted to the study of the influence of the convective unstable nature of the propagating waves on spatio-temporal pattern behavior. Most of the experimental observations are remarkably well reproduced by recent calculations based on coupled Ginzburg–Landau equations

with real coefficients and with the translational term.

Experiments on TW in electroconvecting nematics exhibit a simple scenario of defect nucleation at the transition to complex spatio-temporal behavior. The surprising similarity of spatio-temporal behavior shown by numerical simulations of GGL equation to the experimental observations, suggests that this defect-initiated turbulence is a direct manifestation of BF instability. Thus, it is probably a first step towards universality in spatio-temporal turbulence.

Acknowledgements

This work was supported in part by the US–Israel Binational Science Foundation and the Minerva Foundation.

References

[1] See e.g. Cellular Structures and Instabilities, J. Wesfried and S. Zaleski, eds. Lecture Notes in Physics (Springer, Berlin, 1984).
[2] H. Brand, P.C. Hohenberg and V. Steinberg, Phys. Rev. A 27 (1983) 591; A 30 (1984) 2584 and references cited therein.
[3] K. Nozaki and N. Bekki, Phys. Rev. Lett. 51 (1983) 2171.
[4] H. Brand and V. Steinberg, Phys. Lett. A 93 (1983) 333.
[5] H. Brand and V. Steinberg, Physica A 119 (1983) 327.
[6] E. Knobloch and M.R. Proctor, J. Fluid Mech. 108 (1981) 291.
[7] P. Coullet and B. A. Spiegel, SIAM J. Appl. Math. 43 (1983) 776.
[8] E. Knobloch, Phys. Rev. A 34 (1986) 1539.
[9] H. Brand, P.S. Lomdahl and A.C. Newell, Physica D 23 (1986) 345.
[10] H. Brand, P.S. Lomdahl and A.C. Newell, Phys. Lett. A 118 (1986) 67.
[11] H. Brand and V. Steinberg, Phys. Rev. A 29 (1984) 2303.
[12] C. Bretherton and E.A. Spiegel, Phys. Lett. A 96 (1983) 152.
[13] P. Coullet, S. Fauve and E. Tirapegui, J. Phys. Lett. (Paris) 46 (1985) 787.
[14] I. Rehberg and G. Ahlers, Phys. Rev. Lett. 55 (1985) 560.
[15] R.W. Walden, P. Kolodner, A. Passner and C.M. Surko, Phys. Rev. Lett. 55 (1985) 496.
[16] E. Moses and V. Steinberg, Phys. Rev. A 34 (1986) 1539.
[17] V. Steinberg and E. Moses, in: Pattern, Defects and Microstructures in Nonequilibrium Systems, D. Walgraef, ed., NATO Adv. Study Inst., Series E, Physics (Martinus Nijhoff, Boston, 1987), p. 309.
[18] G. Ahlers and I. Rehberg, Phys. Rev. Lett. 56 (1986) 1373.
[19] T. Sullivan and G. Ahlers, Phys. Rev. Lett. 61 (1988) 78.
[20] T. Sullivan and G. Ahlers, Phys. Rev. A 38 (1988) 3143.
[21] P. Kolodner, A. Passner, C. Surko and R. Walden, Phys. Rev. Lett. 56 (1986) 2621.
[22] C. Surko and P. Kolodner, Phys. Rev. Lett. 58 (1987) 2055.
[23] C.D. Andereck, S.S. Liu and H.L. Swinney, J. Fluid Mech. 164 (1986) 155. R. Tagg and H. Swinney.
[24] V. Croquette and H. Williams, these Proceedings, Physica D 37 (1989) 300.
[25] A. Joets and R. Ribotta, Phys. Rev. Lett. 60 (1988) 2164. I. Rehberg, S. Rasenat and V. Steinberg, Phys. Rev. Lett. 62 (1989) 756.
[26] P. Huerre and P.A. Monkewitz, J. Fluid Mech. 159 (1985) 151.
[27] M. Gaster, J. Fluid Mech. 22 (1965) 433.
[28] M. Gaster, Proc. Roy. Soc. London A 347 (1975) 271.
[29] P. Huerre, in: Instabilities and Nonequilibrium Structures, E. Tirapegi and D. Villarroel, eds. (Reidel, Dordrecht 1987), p. 141.
[30] R. Deissler, Phys. Fluids 30 (1987) 2303.
[31] G.S. Triantafyllou, K. Kupfer and A. Bers, Phys. Rev. Lett. 59 (1987) 1914.
[32] J.M. Chomaz, P. Huerre and L.G. Redekopp, Phys. Rev. Lett. 60 (1988) 25.
[33] E.M. Lifshitz and L.P. Pitaevskii, Physical Kinetics (Pergamon, New York, 1981), p. 268.
[34] M.C. Cross, Phys. Rev. Lett. 57 (1986) 2935.
[35] M.C. Cross, Phys. Rev. A 38 (1988) 3593.
[36] E. Moses, J. Fineberg and V. Steinberg, Phys. Rev. A 35 (1987) 2751.
[37] V. Steinberg, E. Moses and J. Fineberg, Nucl. Phys. B (Proc. Suppl.) 2 (1987) 109.
[38] R. Heinrichs, G. Ahlers and D.S. Cannell, Phys. Rev. A 35 (1987) 2761.
[39] G. Ahlers, D.S. Cannell and R. Heinrichs, Nucl. Phys. B (Proc. Suppl.) 2 (1987) 77.
[40] J. Fineberg, E. Moses and V. Steinberg, Phys. Rev. Lett. 61 (1988) 838.
[41] P. Kolodner and C.M. Surko, Phys. Rev. Lett. 61 (1988) 842.
[42] R.J. Deissler, J. Stat. Phys. 40 (1985) 37; Physica D 25 (1987) 233.
[43] R.J. Deissler and H. Brand, Phys. Lett. A 130 (1988) 293.
[44] T.B. Benjamin, Proc. Roy. Soc. London A 299 (1967) 59.
[45] T.B. Benjamin and J.E. Feir, J. Fluid Mech. 27 (1967) 417.
[46] M. Bestehorn, R. Freidrich and H. Haken, preprint (1988).
[47] I. Rehberg, S. Rasenat and V. Steinberg, Phys. Rev. Lett. 62 (1989) 756.
[48] P. Coullet, L. Gil and J. Lega, preprint (1987).
[49] P. Coullet and J. Lega, preprint (1987).
[50] P. Coullet, et al., these Proceedings, Physica D 37 (1989) 91, and movie presented at this conference.
[51] J. Fineberg and V. Steinberg, Phys. Rev. Lett. 58 (1987) 1332.

[52] J. Fineberg, Ph.D. thesis, Weizmann Institute of Science, Israel (1988), unpublished.
[53] P. Kolodner, H.L. Williams, and C. Moe, J. Chem. Phys. 88 (1988) 6512.
[54] For reviews see W.J.A. Goossens, in: Advances in Liquid Crystals, G.H. Brown, ed. (Academic Press, New York, 1978).
[55] L.M. Blinov, Electro-Optical and Magneto-Optical Properties of Liquid Crystals (Wiley, New York, 1983).
[56] D.T.J. Hurle and F. Jakeman, J. Fluid Mech. 47 (1971) 667.
[57] V. Steinberg, J. Appl. Math. Mech. USSR 35 (1971) 335.
[58] B.J.A. Zielinska and H. Brand, Phys. Rev. A 35 (1987) 4349.
[59] E. Knobloch and D.R. Moore, Phys. Rev. A 37 (1988) 860.
[60] M.C. Cross and K. Kim, Phys. Rev. A 37 (1988) 3909.
[61] P. Kolodner, A. Passner, C.M. Surko and R.W. Walden, Phys. Rev. Lett. 56 (1986) 2621.
[62] C.M. Surko and P. Kolodner, Phys. Rev. Lett. 58 (1987) 2055.
[63] D.R. Caldwell, J. Fluid Mech. 64 (1974) 347.
[64] J. Fineberg and V. Steinberg, unpublished.
[65] P. Coullet, C. Elphick, L. Gil and J. Lega, Phys. Rev. Lett. 59 (1987) 884.
[66] L. Gil and J. Lega, in: Propagation in Systems Far from Equilibrium, J.E. Wesfreid, H. Brand, P. Manneville, G. Albinet and N. Boccara, eds. (Springer, Berlin, 1988), p. 164.
[67] D. Bensimon, B. Shraiman and V. Croquette, preprint (1988).
[68] E. Moses and V. Steinberg, Phys. Rev. Lett. 60 (1988) 2030.
[69] E. Moses and V. Steinberg, these Proceedings, Physica D 37 (1989) 341.
[70] E. Moses, Ph.D. thesis, Weizmann Institute of Science, Israel (1988), unpublished.
[71] M.C. Cross, these Proceedings, Physica D 37 (1989) 315.
[72] J. Fineberg, E. Moses and V. Steinberg, Phys. Rev. A 38 (1988) 9.
[73] We thank P. Kolodner for bringing this point to our attention.
[74] P. Kolodner, comment submitted to Phys. Rev. Lett.
[75] P. Grassberger and I. Procaccia, Phys. Rev. Lett. 50 (1983) 346.
[76] J. Fineberg, E. Moses and V. Steinberg, reply submitted to Phys. Rev. Lett.
[77] A. Newell, private communication.
[78] J.T. Stuart and R.C. Di Prima, Proc. Roy. Soc. London A 362 (1978) 27.
[79] G. Dee and J.S. Langer, Phys. Rev. Lett. 50 (1983) 383.
[80] E. Ben Jacob et al., Physica D 14 (1985) 348.
[81] G. Dee, Physica D 15 (1985) 245.
[82] M. Lücke, M. Mihelcic and K. Wingerath, Phys. Rev. Lett. 59 (1984) 4001.
[83] W. Van Saarlos, Phys. Rev. Lett. 58 (1987) 257.
[84] W. Van Saarlos, Phys. Rev. A 37 (1988) 211.
[85] W. Schöpf and W. Zimmerman, preprint (1988).
[86] P. Kolodner, D. Bensimon and C.M. Surko, Phys. Rev. Lett. 60 (1988) 1723.
[87] A.J. Bernoff, Physica D 30 (1988) 363.
[88] P. Kolodner, C.M. Surko and H. Williams, these Proceedings, Physica D 37 (1989) 319.
[89] A.C. Newell, Lect. Appl. Math. 15 (1974) 157.
[90] L. Gil, J. Lega and J.L. Meunier, to be published.